1

Special Polymers

The properties of some base resins with very few additives other than stabilizers have been discussed in a monograph (1).

Typically, high-performance resins will be used in tough metal replacement applications or replacement of ceramic materials. Thermoset resins are generally highly filled with mineral fillers and glass fibers. Elastomers are polymers that can be stretched substantially beyond their original length and can retract rapidly and forcibly to essentially their original dimensions. Specialty rubbers offer higher performance over general-purpose rubbers and find use in more demanding applications (1).

1.1 Poly(ethylene)

Depending on the temperature, pressure, catalyst, and the use of a comonomer, three basic types of poly(ethylene) (PE) can be produced: high density poly(ethylene), low density poly(ethylene), and linear low density poly(ethylene) (LLDPE) (1).

1.1.1 Metallocene Poly(ethylene)

Unsymmetrical permethylindenyl bent metallocene complexes have been synthesized and reacted with inorganic solid supports to afford catalysts for the slurry phase polymerization of ethylene. Those products, supported on solid polymethylaluminoxane were both highly active catalysts and afforded polymers with a desirable, low aggregation (2).

1.1.1.1 Film Applications

Metallocene catalyzed PE with high and medium densities are known to have good optical properties (3). However, for film applications, they have mechanical properties which can still be improved, in particular dart impact, tear strength and slow puncture resistance. On the other hand, PE prepared with dual site catalysts in the gas phase or with Ziegler-Natta catalysts have good mechanical properties, but poorer optical properties. Nucleating agents are required to improve the gloss and haze. However, nucleating agents are not particularly effective for PE resins. For example, for a haze of 30%, a nucleating agent cannot improve haze to less than 25%.

The preparation of a metallocene-catalyzed PE resin has been reported (3, 4). The metallocene is preferably a bridged unsubstituted bis(tetrahydroindenyl), such as ethylene-bis(tetrahydroindenyl) zirconium dichloride, c.f. Figure 1.1. Triisobutylaluminium can be

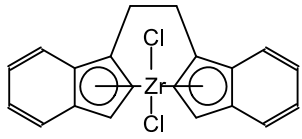

Figure 1.1 Ethylene-bis(tetrahydroindenyl) zirconium dichloride.

used as activating agent.

The polymer has a multimodal molecular weight and composition distribution from 45% to 75% of a low density fraction. This fraction has a density below or equal to 918 $g\,cm^{-3}$ as measured by the the standard test ISO 1183 (5), at a temperature of 23°C., wherein the density of the polyethylene resin is from 0.920 to 0.945 $g\,cm^{-3}$. The M_w/M_n of the polyethylene is of from 2.8 to 6 and the melt index MI2 of the PE resin ranges from 0.1 to 5 $g/10min$.

The described PE resin composition is particularly suitable for film applications i.e. to prepare films. In particular, it shows a good balance in both mechanical and optical properties. In comparison to commercial grades, the mechanical properties are just as good, if not better, with the added advantage that the films obtained using this metallocene-catalyzed PE are particularly transparent i.e. have low haze (3).

1.1.1.2 Brominated Poly(ethylene)

A metallocene-catalyzed copolymerization of ethylene and 11-bromo-1-undecene was carried out to synthesize a brominated PE (6). A modified methylaluminoxane (Methanolato dimethyl aluminium) solution was used as a cocatalyst and ethylene-bis(tetrahydroindenyl) zirconium dichloride, c.f. Figure 1.1, was used as catalyst.

The copolymerization showed a high activity and afforded the copolymer with a 11-bromo-1-undecene incorporation ranging from 1.0 to 4.3 mol-%. When using a dried methylaluminoxane as cocatalyst, the incorporation ratio of 11-bromo-1-undecene increased remarkably to 25.2 mol-%. It was demonstrated that the type of methylaluminoxane used as a cocatalyst can affect the composition of the ethylene 11-bromo-1-undecene copolymer without changing the structure of the catalytic complex (6).

1.1.1.3 Comb-Shaped Materials

Comb-branched ethylene/1-octene copolymer elastomers were synthesized, and their properties were investigated (7).

The polymers had crystalline PE long chain branches attached to amorphous ethylene/1-octene random copolymer backbones. The unique structure was generated through a tandem catalyst system consisting of a Zr ligated with phenoxycycloalkylimine and a constrained geometry catalyst (CGC-Ti). Linear PE macromonomers, with more than 88% of the chains terminally unsaturated, were synthesized with the phenoxycycloalkylimine containing catalyst, while the constrained geometry catalyst catalyst was used in the copolymerization of ethylene, 1-octene, and the PE macromonomer.

The resulting copolymer elastomers possessed high melting temperature of >120°C and a low glass transition temperature of less than −60°C. These properties are suggesting that a phase separation occurred in the copolymer system. The investigation of the mechanical properties showed that the elongation at break reached more than 1200% (7).

1.1.1.4 Shape Memory Polymers

Ethylene vinyl acetate (EVA) was melt-blended with a metallocene

poly(ethylene) elastomer to form shape memory, eco-based blends with and without vinyl triethoxysilane modification (8). Vinyl triethoxysilane is shown in Figure 1.2.

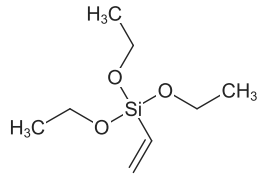

Figure 1.2 Vinyl triethoxysilane.

The silane crosslinking modification slightly suppressed the crystallization temperatures of the metallocene poly(ethylene) component due to the increased gel content. The crystallinity of metallocene poly(ethylene) also decreased slightly, from 4.1% to 1.8%, due to the silane crosslinking effect, and further, to 1.3%, due to the interference effect of EVA.

Despite this negative contribution to thermal crystallization behaviors, the highest tensile strength and Young's modulus were still observed for the EVA/metallocene poly(ethylene)-g-vinyl triethoxysilane blend. This was attributed to the higher interaction between the silane groups on metallocene poly(ethylene) and the vinyl acetate groups on EVA. In addition, the silane grafting modification on metallocene poly(ethylene) improved the thermal stability and shape fixity of the EVA/metallocene poly(ethylene)-g-vinyl triethoxysilane blend further with respect to their corresponding EVA/metallocene poly(ethylene) blend (8).

The recovery ratio of the EVA/metallocene poly(ethylene)-g-vinyl triethoxysilane system was still high, up to 92.8±0.3%, for the recovery from a temporary deformed shape. The shape memory index of the EVA/metallocene poly(ethylene)-*g*-vinyl triethoxysilane blend was about 81%, which was higher than that of the EVA/metallocene poly(ethylene), at about 75%. In particular, the EVA/metallocene poly(ethylene)-*g*-vinyl triethoxysilane could still be melt processed, in comparison with conventional crosslinked shape memory polymer blends which are hard to be recycled (8).

1.1.1.5 *Poly(ethylene)/Carbon Nanotube Nanocomposites*

Nanocomposites,based on a metallocene LLDPE matrix, reinforced with multiwalled carbon nanotubes (CNTs), at various CNT loadings, have been prepared and studied with scanning electron microscopy (SEM), differential scanning calorimetry (DSC), thermal mechanical analysis, tensile-electrical testing, and Raman spectroscopy (9).

A melt-mixing procedure has been applied to prepare the nanocomposites. The employed metallocene LLDPE matrix type was proved to be decisive in producing nanocomposites with improved thermomechanical/electrical properties, due to a good quality dispersion of the CNTs into the specific bulk matrix.

The experimental values of Young's modulus versus the CNT volume fraction are shown in Figure 1.3.

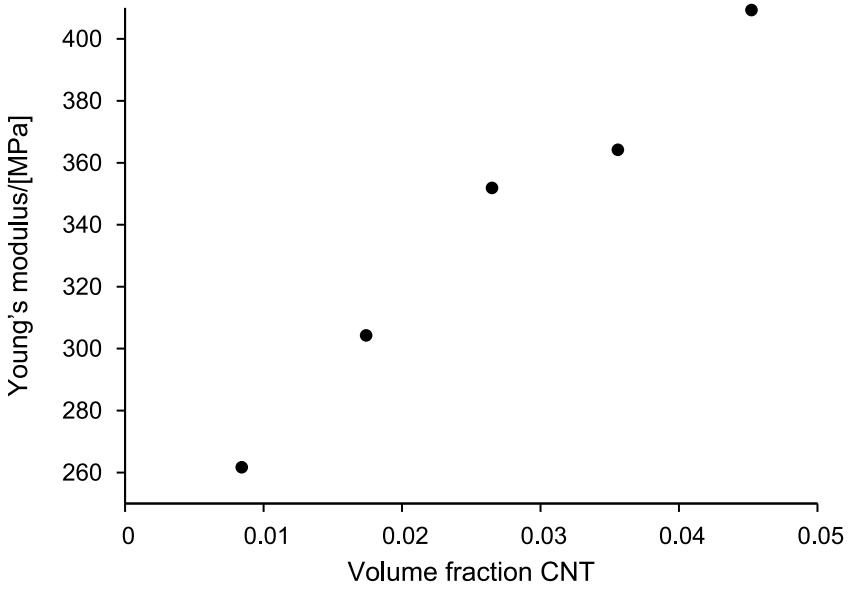

Figure 1.3 Young's modulus versus CNT volume fraction (9).

With regard to the electrical conductivity, two different behaviors with respect to the CNT concentration could be distinguished. The typical behavior of insulating materials where conductivity is frequency dependent in the whole frequency range was observed for pure metallocene LLDPE and for the nanocomposites with a CNT

content of up to 2%. Hereafter, the conductivity plateau is extended in the whole frequency range for a CNT content from 4% to 10%.

Moreover, the electrical conductivity obtained at a specific CNT loading was analyzed by a model relating the electrical resistance of the CNT/nanocomposites with the effective length of CNTs, and the thickness of the interphase between matrix and CNTs. These quantities are parameters which participate in the tunnel effect. The simulated parameter values were in accordance with the results of the micromechanics modelling (9).

1.1.1.6 Antibacterial Coatings

Metallocene PE/nano-silver coatings were prepared by a facile air-spray method on polymer films (10). A metallocene PE sol and nano-silver was used as precursor to deposit coatings on polymers at a relatively low operating temperature. Antibacterial coatings were obtained with excellent mechanical properties, water resistance, and low silver release.

The composite coatings were examined with respect to surface characteristics, mechanical properties, and antibacterial activity against two representative bacterial strains i.e., *Escherichia coli* (E. coli) and *Staphylococcus aureus* (S. aureus). The composite coatings exhibited a favorable microstructure, good mechanical properties, and a suitable crystallinity. The antimicrobial tests indicated that the fabricated composite coatings showed a promising antibacterial activity against E. coli and S. aureus. Furthermore, silver ions released by the composite coating after 30 d were under 1.2 ppb. So, the results of the study indicated a promising prospect of the composite coating for wide antibacterial applications (10).

1.1.2 Geomembranes

A reliable prediction of the service lifetime of tunnel constructions is of essential technical and economic interest (11, 12).

Polymers used for tunnel liners should to fulfill the requirement of 100 y lifetime.

At the moment, reliably proven test methods are available that confirm such long lifetimes of polymers.

A research project which focus on the lifetime prediction of PE for tunnel geomembranes has been reported. Different PE grades in combination with different antioxidant packages were conditioned at elevated temperatures and different media. Initial results confirmed a significant material aging already after an exposure up to 16 weeks, at least at the highest exposure temperature of 800°C.

To consider application relevant material properties, the material characterization was done by means of tensile tests and dynamic oxidation induction temperature tests. High performance liquid chromatography was used for further investigation of antioxidant consumption kinetics (11).

1.2 Poly(styrene)

The three main categories of commercial poly(styrene) (PS) resins are crystal PS, impact PS, and expanded PS foam (1).

Engineering thermoplastics comprise a special performance segment of synthetic plastics materials that offer enhanced properties (1).

1.2.1 Syndiotactic Poly(styrene)

A semicrystalline styrene polymer has been produced by metallocene catalysis (13).

Syndiotactic poly(styrene) (SPS) is a semi-crystalline polymer developed by Dow Plastics (14). The material is completely different from conventional styrene polymers in structure, physical properties and synthetic method. It represents the basis for an entirely new family of materials based on crystalline PS.

SPS has a melting point of 270°C combined with an excellent resistance to moisture and automotive fluids. Additionally, SPS products exhibit exceptional electrical performance and competitive toughness and stiffness. A wide range of products have been formulated for specific applications including impact-modified and glass-reinforced grades.

The attributes of SPS as they relate to use of this material in automotive, interconnect systems where a combination of heat resistance, chemical resistance, dimensional stability and enhanced

processability have been discussed. Specific topics include the characterization of the indirect IR soldering resistance of formulated SPS compounds when molded into interconnect devices, as well as the processability and performance of this class of materials (14).

1.2.1.1 *Amino-containing Polymers*

Amino-containing functionalized SPS with high melting temperatures and a high temperature stability were synthesized by the direct polymerization of amino-containing styrenic monomers in the presence of a half-sandwich scandium catalyst system (15). The reaction is shown in Figure 1.4.

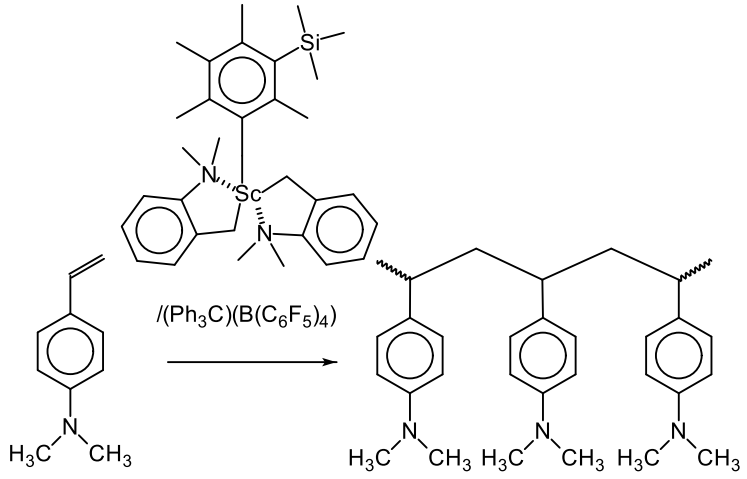

Figure 1.4 polymerization of amino-containing styrenic monomers (15).

The high syndiotactic poly(*N*,*N*-dimethylamino)styrene could be used as polymer supports, effectively anchored Pd nanoparticles with 3% of Pd, with a diameter of 4 *nm* or 5 *nm* that could be uniformly dispersed on the polymer matrix (15).

1.2.1.2 *Styrene Ethylene Copolymers*

The syndiotactic polymerization of styrene and the copolymerization of styrene with ethylene were carried out by using a series

of chiral half-sandwich rare-earth metal dialkyl complexes as catalysts (16).

In comparison to titanium complexes, the advantage of these half-sandwich rare-earth metal complexes is that they can promote the copolymerization of styrene with ethylene, yielding random copolymers that are containing syndiotactic polystyrene sequences (17, 18).

Such styrene ethylene copolymer can overcome the drawbacks of SPSs, such as brittleness and poor processing performance due to its high melting temperature, and so broaden its industrial applications (19).

The cationic half-sandwich scandium alkyl catalysts were synthesized by a procedure described in the literature (20).

The resulting SPSs showed molecular weights (M_n) ranging from 3700 $g\,mol^{-1}$ to 6400 $g\,mol^{-1}$ with molecular weight distributions (M_w/M_n) from 1.40 to 5.03 (16).

The bulky cyclopentadienyl ligands of the chiral half-sandwich rare-earth metal complexes effectively inhibit the continued insertion of styrene monomers into the (co)polymer chain to some extent in comparison with the known half-sandwich rare-earth metal complexes (16).

1.2.1.3 Styrene Terpene Copolymers

The copolymerization of bio-renewable β-myrcene or β-farnesene with styrene was examined using an ansa-neodymocene catalyst, affording two series of copolymers with high styrene content and unprecedented syndioregularity of the PS sequences (21). The terpenes are shown in Figure 1.5.

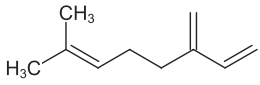

β-Myrcene

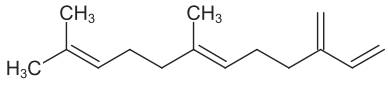

β-Farnesene

Figure 1.5 Terpenes.

The incorporation of terpene in the copolymers ranged from 5.6 to 30.8 mol-% (β-myrcene) and from 2.5 to 9.8 mol-% (β-farnesene), respectively. Nuclear magnetic resonance spectroscopy spectroscopy and DSC suggested that the microstructure of the copolymers consists of 1,4- and 3,4-poly(terpene) units randomly distributed along syndiotactic polystyrene chains.

The thermal properties of the copolymers are strongly dependent on the terpene content, which is easily controlled by the initial feed. The terpolymerization of styrene with β-myrcene in the presence of ethylene was also examined (21). The remarkably narrow and monomodal molecular weight distributions suggested the formation of true terpolymers.

1.2.1.4 Thermal Conductivity

In cocontinuous conductive polymer composites that are designed for heat generation by the Joule effect, the thermal conductivity of the electrically insulating matrix is the limiting factor to get a good heat dissipation (22).

To prevent the establishment of a non desirable high temperature gradient in the heating elements, it is necessary to enhance the thermal conductivity of the composite independently from its electrical conductivity. Several adequate fillers for this purpose are known, such as boron nitride, talc, aluminum nitride, and aluminum oxide particles. Their impact on the thermal properties and SPS phase transition temperatures have been studied.

Lewis and Nielson, Cheng and Vachon, Agari and Uno models were used to predict the evolution of thermal conductivity with filler content (22). These models were found to describe correctly thermal conductivity of the materials after the determination of the maximum packing fraction, the shape factor, parameters of modifications of crystals and the ability of the filler particles to associate into chains. These models show that whatever the filler and unlike electrical conductivity, thermal conductivity does not go through a sharp insulator/conductor (percolation threshold).

Only boron nitride showed a real exponential increase of conductivity over 20% v/v filler. Consequently, in best conditions introducing 30% v/v of boron nitride allows the thermal conductivity to be multiplied by six. Boron nitride particles were also found

to shift the conductive polymer composites glass transition temperature, the non-isothermal crystallization temperature, and the melting temperature (22).

1.3 Poly(ethylene terephthalate)

1.3.1 Blends of Poly(ethylene terephthalate) and Poly(phenylene sulfide)

The thermal and crystallization behavior of blends of glass fiber reinforced poly(phenylene sulfide) (PPS) with poly(ethylene terephthalate) (PET) has been reported (23).

The blends showed two overlapping melting peaks and two separate crystallization peaks. The heat of crystallization of PPS was found to decrease continuously with increasing PET content, whereas the heat of crystallization of PET was found to increase with increasing PPS content.

This indicates that the degree of crystallinity of PPS is reduced whereas that of PET is increased as a result of blending. The combined heats of fusion of the blends were marginally higher than those calculated by the proportional additivity rule in spite of the drop in the heat of crystallization of PPS. The temperature onset of crystallization of PET in the blends shifted to higher temperature whereas there was no significant change in the crystallization temperature of PPS. The increase in the temperature of crystallization of PET indicates enhanced nucleation.

Isothermal crystallization studies of the component polymers revealed that both the component polymers crystallized at a relatively faster rate in the blend. The crystallization rate of PPS was found to increase significantly with increasing PET content. A significant increase in the rate of crystallization of PET was also observed in the blends. The acceleration of the crystallization rate of PET in the blends was more pronounced in comparison to that of PPS. The acceleration in the PET crystallization rate was attributed to the presence of glass fibers and crystallized PPS (23).

1.4 Silicones

1.4.1 Silicon Nanocrystals and Silicon-Polymer Hybrids

Silicon nanocrystals are emerging as an attractive class of quantum dots owing to the natural abundance of silicon in the Earth's crust, their low toxicity compared to many Group II–VI and III–V based quantum dots, compatibility with the existing semiconductor industry infrastructure, and their unique optoelectronic properties (24). Despite these favorable qualities, silicon nanocrystals have not received the same attention as Group II–VI and III–V quantum dots, because of their lower emission quantum yields, difficulties associated with synthesizing monodisperse particles, and oxidative instability.

Recent advancements indicate the surface chemistry of silicon nanocrystals plays a key role in determining many of their properties. A review has been presented that summarizes new reports related to engineering silicon nanocrystal surfaces, synthesis of silicon nanocrystal/polymer hybrids, and their applications in sensing, diodes, catalysis, and batteries (24).

1.4.1.1 Humidity Sensor

A fast-response and flexible nanocrystal-based humidity sensor has been developed for real-time monitoring of human activity, e.g., respiration and water evaporation on skin (25).

A silicon-nanocrystal film is formed on a polyimide film by spin-coating the colloidal solution and is used as a flexible and humidity-sensitive material in a humidity sensor. The flexible nanocrystal-based humidity sensor shows a high sensitivity; current through the nanocrystal film changes by 5 orders of magnitude in the relative humidity range of 8–83%. The response/recovery time of the sensor is 40 *ms*. Due to the fast response and recovery time, the sensor can monitor human respiration and water evaporation on skin in real time. Also, due to the flexibility and the fast response/recovery time, the sensor is promising for its application in personal health monitoring as well as environmental monitoring (25).

1.4.2 Surfactants

Silicone based surfactants have been detailed in a monograph (26).

Organosilicon surfactants are the most potent adjuvants available for formulating and applying agricultural pesticides and fertilizers, household cleaning and personal care products, dental impressions and medicines (27).

Over a billion pounds of organosilicon surfactants for all uses are produced globally per year, making this a major component of the chemical landscape to which bees and humans are exposed. These silicones are generally recognized as safe, have no mandated tolerances, and their residues are largely unmonitored. The lack of their public disclosure and adequate analytical methods constrains evaluation of their risk.

The impacts of organosilicon surfactant exposures on humans need to be evaluated. Silicones in their great diversity probably represent the single most ubiquitous environmental class of global synthetic pollutants (27).

1.4.2.1 Anionic Silicone Surfactants

3-Tris(trimethylsiloxy)silylpropyl sulfonate, c.f. Figure 1.6, with different alkaline counterions (lithium, sodium, and potassium), were synthesized (28).

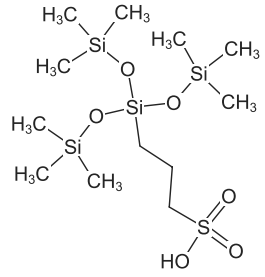

Figure 1.6 3-Tris(trimethylsiloxy)silylpropyl sulfonate.

These anionic silicone surfactants exhibit a remarkable surface activity and can reduce the surface tension of water to as low as 19.8 $mN\,m^{-1}$ at the critical aggregate concentration. The adsorption

and aggregation behaviors of these surfactants were assessed by determining the adsorption efficiency, minimum average area per surfactant molecule, and thermodynamic parameters.

The lowest surface tension, the smallest critical aggregate concentration value, and the largest aggregate size have been reached with potassium counterions. Thus, the different behavior of these surfactants in water can be explained by the different sizes of the hydrated ions (28).

1.4.2.2 Lubricating Substances

Standard lubricating substances are usually based on mineral oils (29). These compounds, however, fail to meet a range of criteria that are required of modern lubricants. Mineral oils are not biodegradable and are considered a threat to the environment and humans. The majority of standard lubricating oils contain antiwear additives, including organic sulfur compounds, organoboron derivatives, organometallic derivatives, and organic compounds of chlorine. An improvement in antiseizure properties is often achieved with the addition of alkyl derivatives of dithiophosphates, dithiocarbamates, phosphosulfurized hydrocarbons, chlorinated paraffins, and organometallic compounds.

The most common friction modifier additives added to the base lubricants include fatty acids and amines, fatty acid esters, dialkyldithiophosphates, metal dialkyldithiocarbamates, and organic compounds of copper. This group of additives also includes solid lubricants: molybdenum sulfide and graphite.

The physicochemical and tribological properties of silicone polyether aqueous solutions were investigated (29). The raw materials used in this research were characterized by different oxyethylation and oxypropylation degrees. The raw materials were characterized by different degrees of polymerization of the siloxane chain (m, n) and different degrees of oxyethylation (x) and oxypropylation (y): PEG/PPG-20/20 dimethicone (degrees of polymerization m = 32, n = 6), bis-PEG/PPG-20/20 dimethicone (m = 62, n = 0), and PEG/PPG-25/25 dimethicone (m = 38, n = 3).

It was found that oxyethylated and oxypropylated silicone aqueous solutions, particularly at higher concentrations of 60% to 80%,

and pure compounds can be used as potential and effective lubricants (29).

1.4.2.3 Gemini Surfactants

In recent years, gemini surfactants have drawn extensive attention, due to their fascinating properties over conventional surfactants, single tail/single head surfactants (30–32).

Compared with traditional surfactants, gemini surfactants show a lower critical micelle concentration, higher surface activity and multifarious aggregate structures (33). Owing to these unique properties, they exhibit better wetting, emulsification and solubilization capabilities (34),

1.4.2.4 Textile Washing

The application of trisiloxane polyether silicone surfactant to remove various stains along with a range of hydrocarbon (organic) surfactants has been detailed (35).

It was investigated, whether silicone surfactants offer a synergism or an antagonism during a cotton fabric cleaning process. The cotton fabric was soiled with red wine, turmeric, permanent marker, acrylic paint, and coffee and washed with the original fabric in aqueous solutions of individual surfactant and blend of surfactants by applying the conventional shaking washing method.

The detergency and the soil redeposition were determined from the alteration in the surface reflectance of prepared stained fabrics and the original fabric after washing.

Surfactants used for the washing were a trisiloxane polyether silicone surfactant (AG-Platinum), sodium dodecyl benzene sulfonate, lauryl alcohol ethoxylate, and nonylphenol ethoxylate, and blends of these compounds (35). These compounds are shown in Figure 1.7.

In comparison to individual hydrocarbon surfactants, blends of surfactants, with different hydrocarbon to silicone surfactant ratios, dislodged stains (accumulated on the fabric as a result of staining) effectively at shorter time and at lower bath ratio, because of superior surface properties.

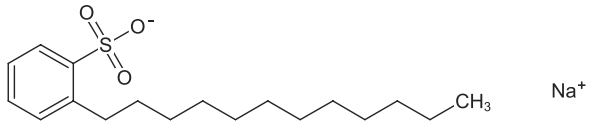

Sodium dodecyl benzene sulfonate

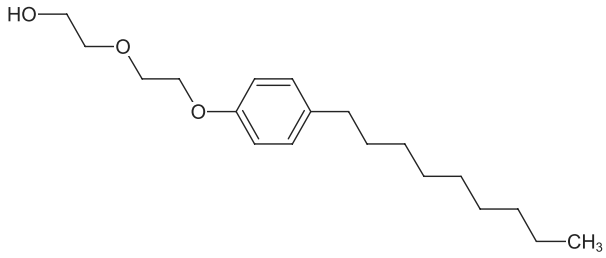

Nonylphenol ethoxylate

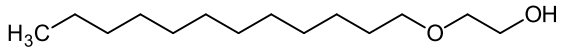

Lauryl alcohol ethoxylate

Figure 1.7 Surfactants.

With increasing concentration of the surfactant, the detergency increased and reached a maximum at the critical micelle concentration. The silicone surfactant reduced the critical micelle concentrations of the surfactant blends and provided a better detergency at a lower concentration. So, it was found that silicone surfactant could be successfully introduced into laundry detergent formulations (35).

1.4.2.5 Metal Extraction

Two cationic silicone surfactants, 3-[tri-(trimethylsiloxy)] silylpropylpyridinium chloride (Si4pyrCl) and *N*-methyl-3-[tri-(trimethylsiloxy)] silylpropylpiperidinium chloride (Si4pipCl), were synthesized. These compounds are shown in Figure 1.8,

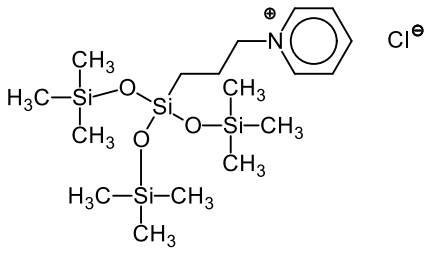

3-[Tri-(trimethylsiloxy)] silylpropylpyridinium chloride

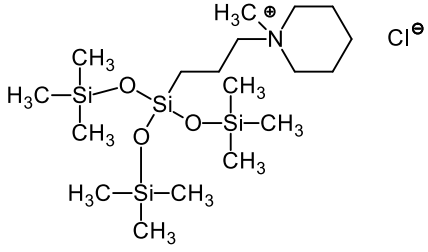

N-methyl-3-[tri-(trimethylsiloxy)] silylpropylpiperidinium chloride

Figure 1.8 Cationic silicone surfactants.

Their aggregation behavior in aqueous solution was investigated through surface tension, electrical conductivity, dynamic light scattering, and transmission electron microscopy (TEM).

The measurements of the surface tension showed that the two cationic silicone surfactants decreased the surface tension of water to almost 20 $mN\,m^{-1}$. This result indicated the remarkable surface activity of the surfactants.

The effects of inorganic salts, sodium chloride, sodium bromide, sodium iodide and sodium sulfate, on the aggregation behavior of the silicone surfactants were explored. The results showed that the aggregation of the silicone surfactants was promoted by the addition of salts and that the aggregation ability followed the order of NaI>NaBr>Na2SO_4>NaCl.

Spherical aggregates with diameters ranging from 200 *nm* to 600 *nm* were observed by TEM, and the aggregates' diameter distribution was obtained by dynamic light scattering.

The extraction behavior on several metal ions (Co (II), Mn (II), Fe (III), Ni (II), Cu (II), Al (III), Sn (IV), Zn (II), Ce (III), Li (I), Mg (II), Au (III), and Pd (II)) in chloroform by the surfactants in chloroform was studied. The results showed that the surfactants showed a good extraction ability for Au (III) and Pd (II) (36).

1.4.2.6 Smithsonite Flotation

A cationic organic silicone surfactant (DTA) with specially designed functional groups was developed as a flotation collector for smithsonite (37). This surfactant was synthesized via the reaction between hexaethyldisiloxane and *N*-β-(aminoethyl)-γ-aminoisobutylmethyldimethoxy silane using tetramethylammonium hydroxide as a catalyst. The steps are shown in Figure 1.9.

The flotation performance was validated by flotation tests using pure minerals. The results illustrated that DTA has strong collecting ability and better selectivity for smithsonite against quartz, calcite and dolomite compared to the traditional collectors such as octadecylamine, tetradecylamine and dodecylamine.

Based on the analysis of fourier transform infrared spectroscopy (FTIR) spectra, zeta-potential measurements, X-ray photoelectron spectroscopy and density functional theory calculations, it can be concluded that the adsorption mechanism of DTA on the surface of smithsonite was mainly dominated by chemisorption and electrostatic adsorption.

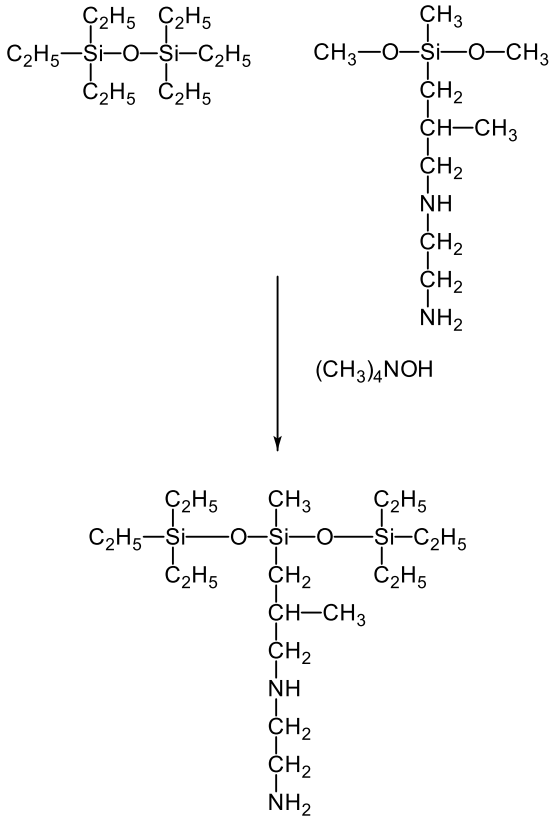

Figure 1.9 Synthesis silicone surfactant (37).

These unique properties of DTA, result in superior collecting powers for smithsonite (37).

1.4.2.7 Methane Hydrate Formation

Recently, the storage of methane in its solid hydrate form has become a rather attractive and low risk option for the storage large amounts of this gas owing to its mild storage conditions, high gas retention capacity and benign (non-explosive) character (38). However, there is a slow rate of hydrate formation, which makes problems for this technique.

The addition of surfactants, like sodium dodecyl sulfate, to the hydrate forming system significantly speeds up the process of methane hydrate formation. but here, a large amount of foam is generated by these surfactants during the process of hydrate formation.

In a study, a small amount of a silicon based surfactant has been proposed to be used as an antifoam agent in conjunction with an anionic surfactant, i.e., sodium dodecyl sulfate, to eliminate the foam generation and to promote the kinetics of the formation of methane hydrate (38). The silicone based antifoam containing 100% active silicone polymer is available from Sigma-Aldrich as Antifoam-A Concentrate.

The optimum ratio in which sodium dodecyl sulfate and Antifoam-A should be mixed is 1% dodecyl sulfate and 0.5% Antifoam-A in order to obtain a maximum foam suppression (38).

1.4.2.8 Foams

Poly(urethane) Foams. Silicone surfactants for their use in poly(urethane) (PU) foams have been described (39). The silicone surfactants have dimethyl siloxane backbones with attached alkyl and polyether pendant groups that provide improved properties for flexible urethane foam compositions.

Specific silicone foam stabilizers that can be used herein include Niax® silicones L-635, L-620 and SC-154, all available from GE Advanced Materials, Silicones (40).

Foam Combinations. Silicone surfactants can be used in combination with hydrocarbon surfactants.However, the properties of the mixtures of silicone and hydrocarbon surfactants have received little attention, especially the foam properties of such mixtures.

Aqueous solutions of binary mixtures of a nonionic silicone surfactant with anionic, cationic, and nonionic hydrocarbon surfactants were prepared for the evaluation of their foam properties (41).

As silicone surfactant, a poly(oxyethylene trisiloxane) compound was used. This material is shown in Figure 1.10.

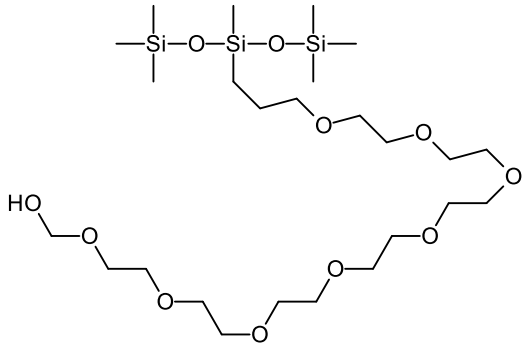

Figure 1.10 Poly(oxyethylene trisiloxane).

The surface tension of aqueous solutions of the mixtures were measured with the maximum bubble pressure method.

The variation of the surface tension with the concentration of surfactant is shown in Figure 1.11.

The foaming ability and the foam stability of these mixtures were evaluated using the standard Ross-Miles method (41).

It was shown that the addition of the silicone surfactant results in a decrease in surface tension for aqueous solutions of the hydrocarbon surfactants.

The critical micelle concentration of the hydrocarbon surfactants is also changed by the additive silicone surfactant (41).

In addition, clear foam synergistic effects were observed in the mixtures of silicone and hydrocarbon surfactants, regardless of the ionic types of the hydrocarbon surfactant. The foam stability of the hydrocarbon surfactant was shown to generally improve with the increasing concentration of the silicone surfactant.

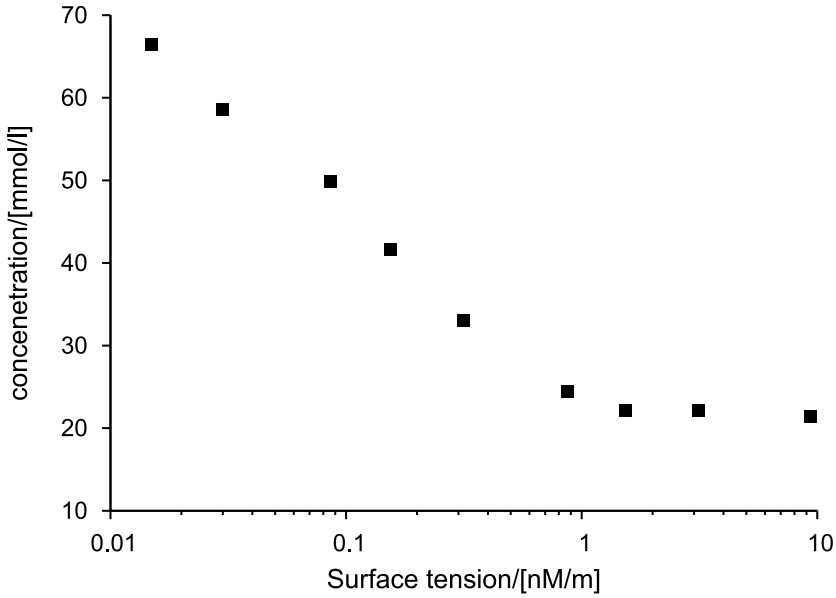

Figure 1.11 Variation of the surface tension with the concentration of surfactant (41).

Aqueous solutions containing different ionic hydrocarbon surfactants in the presence of the silicone surfactant are giving different foam stabilities (41).

Antibacterial Activity. Silicone surfactants are used in a variety of applications, however, only limited knowledge is available on the relationship between surfactant structure and biological activity. It is known that some silicones, including superwetters, exhibit biological activity.

A series of seven nonionic, silicone polyether surfactants with known structures was tested for *in vitro* antibacterial activity against *Escherichia coli* BL21 (42, 43).

Compounds Si10-PEG44, Si4Ph6-PEG44, Si7-PEG15, Si7-PEG44, Si4Ph3-PEG15, Si4Ph3-PEG44 and Si4-PEG44 were prepared according to procedure of Grande (44). Some compounds are shown in Figure 191107.14.50.

The nomenclature is as follows: SiX, where X is the number of siloxane units. If Si-phenyl groups are present their number is in-

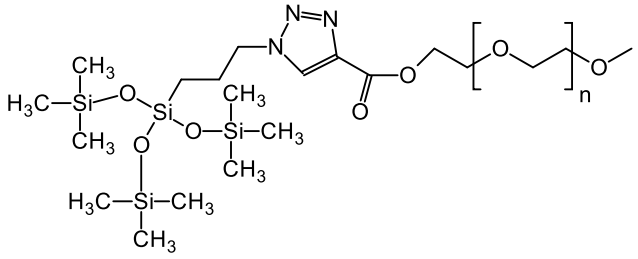

Si4PEGn

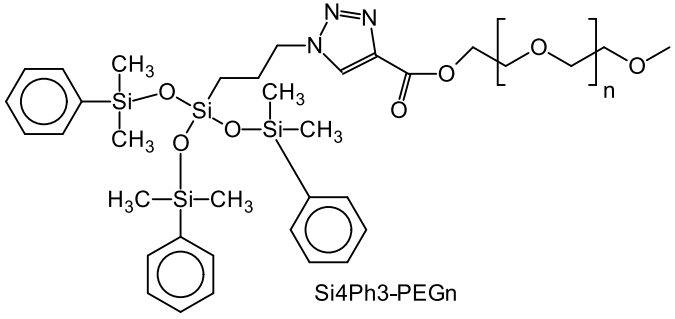

Si4Ph3-PEGn

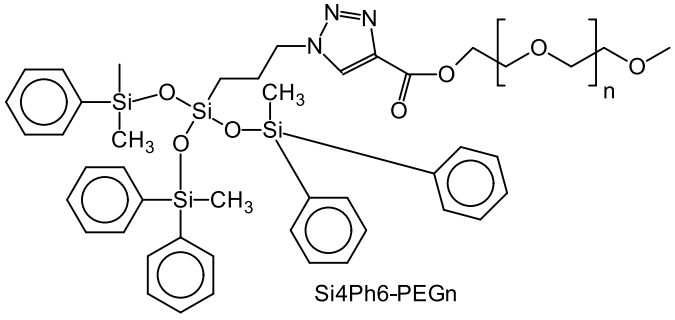

Si4Ph6-PEGn

Figure 1.12 Si4-PEGn, Si4Ph3-PEGn, Si4Ph6-PEGn.

dicated with PhY, Y = 3 or 6; PEGn, where n is the number of $-OCH_2CH_2-$ units in the surfactant)

The compounds varied in their hydrophobic head, comprised of branched silicone structures with 3–10 siloxane linkages and, in two cases, phenyl substitution, and hydrophilic tail of 8–44 poly(ethylene glycol) units.

The surfactants were tested at three concentrations: below, at, and above their critical micelle concentrations (CMC) against 5 concentrations of E. coli BL21 in a three-step assay comprised of a 14–24 *h* turbidometric screen, a live-dead stain and viable colony counts. The bacterial concentration had little effect on antibacterial activity. For most of the surfactants, the antibacterial activity was higher at concentrations above the critical micelle concentration. Surfactants with smaller silicone head groups had as much as 4 times the bioactivity of surfactants with larger groups, with the smallest hydrophobe exhibiting potency equivalent to sodium dodecyl sulfate.

Smaller poly(ethylene glycol) chains were similarly associated with higher potency. These data link lower micelle stability and enhanced permeability of smaller silicone head groups to antibacterial activity. The results demonstrate that simple manipulation of nonionic silicone polyether structure leads to significant changes in antibacterial activity (42).

The adhesion of *Escherichia coli* to copolymers of methacrylates and a trisiloxane-polyether acrylate surfactant was found to be at a minimum with copolymers containing a low fraction of the surfactant monomer of 20%. Rather than wettability, hardness, or water uptake, adhesion was found to be limited by the presence of low concentrations of the bound surfactant that can interact with hydrophobic domains on the bacterium inhibiting anchoring to the polymer surface (45).

A series of cationic silicone surfactants containing ester groups and double long-chain alkyl groups were synthesized by microwave irradiation (46). The surface activity and the adsorption of these surfactants were investigated by measuring the equilibrium surface tension. The critical micelle concentration decreased with increasing length of the alkyl groups.

It could be shown that the cationic silicone surfactants exhib-

it certain antibacterial properties against *Staphylococcus aureus* but slightly poor to *Escherichia coli* (46).

When cotton fabrics were treated with the cationic silicone surfactants, the finished cotton fabrics maintained some antibacterial properties with improved softness, which may provide a more comfortable and healthy lifestyle (46).

1.5 Self-healing Polymers

Self-healing materials are artificial or synthetically-created substances which have the built-in ability to automatically repair damage to themselves without any external diagnosis of the problem or human intervention (47).

Although the most common types of self-healing materials are polymers or elastomers, the self-healing property covers all classes of materials, including metals, ceramics, and cementitious materials (47).

The issues of self-healing polymers have been described in several monographs (48–51).

Progress toward inexpensive, strong, and tunable self-healing materials will significantly accelerate their adoption into commercial applications. This area of research has been under intense investigation and many strategies for the design of self-healing materials have emerged recently (52, 53)

One self-healing approach is to store the reactive healing agents in the material (54–56),

or delivering them via vasculature network to the damage site (57, 58).

Programmed shape memory transitions are investigated to physically close the damaged gap and facilitate polymer diffusion across the cut interfaces and subsequent healing (59).

Additionally, significant efforts have been directed at the discovery of new intrinsically self-healing polymers to design materials that can efficiently repair themselves after multiple cycles of damage. During the last decade, many new covalent bonds (i.e. metathesis of double bonds (60), disulfide bond exchange (61), thiuram disulfide (62), siloxane exchange (63), exchange of catechol-based boronic ester (64), Diels-Alder reaction (65).

Also, non-covalent interactions (66) have been explored as dynamic motif.

Supramolecular interactions, such as metal-ligand (67, 68), host-guest (69), π-π stacking (70), ionic (71), hydrogen bonds (72), have been also a subject of intensive investigation since the broad tunability of their kinetic and thermodynamic parameters can be productively utilized to control mechanical and self-healing properties (73).

The development of self-healing systems utilizing dynamic interactions (60, 74–76) has been demonstrated.

1.5.1 Multiphasic Copolymer

A multiphasic copolymer that phase separates into glassy domains with a high glass transition temperature, embedded in a matrix of dynamic non-covalent interactions, H-bond or metal-ligand interactions, with high mobility is a promising route to combine efficient self-healing and strong mechanical properties (77, 78).

A multiphase copolymer with *n*-butyl acrylate and an acrylamide monomer is addressed as BAAM copolymer. The synthesis of a BAAM copolymer is shown in Figure 1.13.

Here, the polymer segment can include polymerized styrenic or acrylic monomer segments forming glassy domains in the multiphase copolymer (78). The multiphase copolymer can be a linear copolymer or a branched copolymer. The polymerized acrylamide monomer includes functional groups that form hydrogen bonds in the multiphase copolymer, and is present in the one or more copolymer segments in an amount sufficient for self-healing of the multiphase copolymer.

This multiphase approach overcame one major obstacle to realizing the wide spread use of self-healing polymers utilizing non covalent, dynamic interactions. By introducing a discontinuous glassy hard phase (to improve stiffness and yield strength) covalently connected to a continuous soft phase bearing a robust network of dynamic motifs, the inherent trade-off between stiff low-strain mechanical response and stimulus-free dynamic self-healing was circumvented to effect nearly quantitative self-healing after catastrophic macroscopic damage (77).

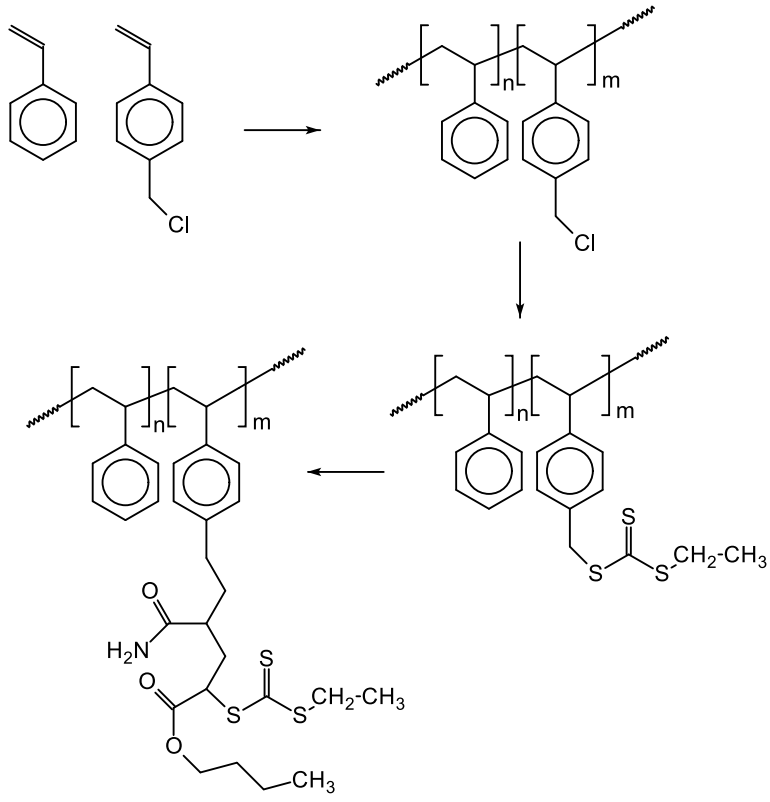

Figure 1.13 Synthesis of BAAM copolymers (78).

1.5.2 Hydrophobic Coatings

A synthetic strategy was developed for a hydrophobic and self--healing anticorrosion coating from carboxylic acid- and fluorine-containing nanocontainers (79).

Poly(acrylic acid-*co*-trifluoroethyl methacrylate) microspheres were synthesized with different crosslinking agents by a distillation precipitation polymerization (80). Trifluoroethyl methacrylate is shown in Figure 1.14.

The carboxylic acid groups allow for pH-responsive function to control the release of the encapsulated healing inhibitor to the cracks of polymer coatings on metal surfaces. The fluorinated groups of the polymer nanocontainers can endow the coatings with hydrophobicity. The synthesized multifunctional nanocontainers were further doped into the polymer coatings to generate self-healing coatings.

The self-healing polymer coatings exhibited a good crack inhibition since the inhibitor 1,2,3-benzotriazole, c.f. Figure 1.14, in pH-responsive nanocontainers can autonomously form new nanobarriers on metal surfaces around cracks after corrosion occurs. Furthermore, due to the micro/nanostructures of hydrophobic microspheres in the polymer coatings, the self-healing coating also exhibited a good water resistance (79).

Trifluoroethyl methacrylate 1,2,3-Benzotriazole

Figure 1.14 compounds for fluorine-containing nanocontainers.

1.5.3 Microcapsule Based Self-Healing

Microcapsule based self-healing has emerged as a powerful tool for autonomic damage mitigation in polymers (81). Such self-healing polymers are extremely attractive for a number of applications.

In conventional self-healing polymers, catalyst particles and liquid monomer-containing microcapsules are embedded in a base polymer for which healing is desired. Upon damage, the microcapsules are ruptured, releasing liquid monomer into the damage volume, which subsequently polymerizes when in contact with the catalyst particles, thereby adhering the damage surfaces without the need for manual intervention (81).

Electrical wires generally contain an inner metal conductor surrounded by an insulation material (82). The insulation becomes more brittle with age, and can crack or develop defects due to age, heat, exposure to strong electrical fields, and friction with other wires or surrounding objects or surfaces. Problems in electrical wiring systems are an important threat to the safety of spacecraft and aircraft, as well as other electrical devices.

Poly(imide)s (PIs) are high performance polymers that have been used as wire insulation in demanding applications that have low tolerance for failure, such as space travel and aeronautics. The standard wire insulation for spacecraft and aircraft is PI, particularly Kapton®. PIs have excellent an thermal stability and strength.

Wire insulation with a built in self-healing capability would improve the safety of systems containing electrical wiring. Such insulation would require less inspection and repair time over the lifetime of the system.

A polymer material has been developed tat is containing a low-melt polymer matrix that melts at a temperature below 300°C and a first set of microcapsules containing an outer wall and an inner compartment, wherein the inner compartment is a volatile solvent that when released from the microcapsules melts or softens the polymer matrix (82).

1.5.4 Tunable Mechanical Strengths

The development of self-healing polymers with tunable mechanical performances is an enormous challenge. Self-healing polymers with tunable mechanical strengths via combined hydrogen bonding and Zn(II)-imidazole interactions could be successfully synthesized (83).

This synthesis was accomplished by introducing urea hydrogen bonding and Zn(II)-imidazole interactions into self-healing polymers polymerized from a bifunctional monomer of

2-(3-(3-imidazolylpropyl)ureido)ethyl acrylate. This monomer is shown in Figure 1.15.

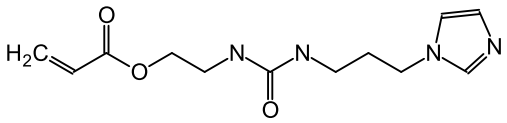

Figure 1.15 2-(3-(3-Imidazolylpropyl)ureido)ethyl acrylate.

The dual dynamic effects of urea hydrogen bonding and Zn(II)-imidazole interactions can simultaneously endow polymers with better self-healing capacities and mechanical properties. The synthesized polymers with urea hydrogen bonding and Zn(II)-imidazole interactions motifs exhibited over 90% self-healing efficiency under mild conditions. The mechanical strengths of the polymers can be flexibly tuned from 35.0 *kPa* to 4.41 *MPa* by varying the molar ratio of imidazole/Zn(II).

When the polymers are becoming damaged, the urea hydrogen bonds and the Zn(II)-imidazole coordination can contribute to the reconstruction of the broken polymer networks and thus provide self-healing abilities (83). The interactions of hydrogen bonding and Zn(II)-imidazole coordination could be confirmed by in situ FTIR spectra of the self-healing polymers at different temperatures.

1.5.5 Bioinspired Pathways

1.5.5.1 Leaf-Inspired Polymers

Hierarchical multiphase fibrous morphologies provide the strength and the elasticity of biological species, thus facilitating their responses to environmental changes. One example is the wound closure of leaves (84).

If polymers can be formed in a similar manner by introducing multiphase-separated morphologies, self-healing in a variety of commodity materials can be achieved. In these studies, we demonstrate the role of phase morphologies, interphases, and viscoelasticity-driven shape memory effects on self-healing. Self-healing can be

repeated many times. This behavior is attributed to the shape memory effect, given that a micron-scale interphase reduces chain slippage, enabling entropic energy storage during damage. Chemically identical but nanophase-separated copolymers do not exhibit this behavior.

Phase-separated poly(caprolactone) (PCL)-PU fibrous thermoplastic polymers were synthesized, in which the microphase separation facilitates the formation of stable interfacial regions between hard and soft segments (84).

The polymers are containing a soft block and a hard block. As a soft block a spiropyran mechanophore and a PCL soft segment is used. As a hard segment, a 1,4-butandediol block is used. The spiropyran mechanophore is containing a hydroxyl modified spiropyran, c.f. Figure 1.16.

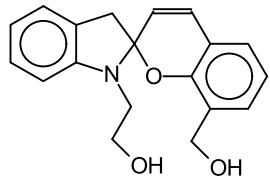

Figure 1.16 Spiropyran mechanophore (84).

1.5.5.2 Imidazole-Metal Coordination

Chemical level design principles extracted from proteinaceous biopolymers, especially the mussel byssus, are providing an inspiration for the design of autonomous and intrinsic healing in synthetic polymers (85). The mussel byssus is an acellular tissue comprised of extremely tough protein-based fibers, produced by mussels to secure attachment on rocky surfaces.

Threads exhibit self-healing response following an apparent plastic yield event, recovering initial material properties in a time-dependent fashion. Recent biochemical analysis of the structure-function relationships defining this response reveal a key role of sacrificial cross-links based on metal coordination bonds between Zn^{2+} ions and histidine amino acid residues. Histidine is shown in Figure 1.17.

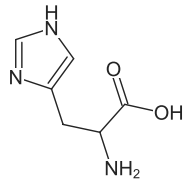

Figure 1.17 Histidine.

Inspired by this example, many research groups have developed self-healing polymeric materials based on histidine (imidazole)-metal chemistry.

A detailed overview of the current understanding of the self--healing mechanism in byssal threads has been given (85), and also an overview of the current state of the art in histidine- and imidazole-based synthetic polymers.

Many different metal-ligand interactions have been implemented into synthetic polymers as versatile building blocks (86).

These materials, the so-called metallopolymers, are a subclass of the rich family of supramolecular polymers. Metallopolymers combine both structural elements, i.e., metal complexes and polymers, within a single material. Consequently, they also feature the corresponding properties derived from both subunits (85).

1.6 Fibers and Smart Polymers

1.6.1 Natural Fiber Reinforced Polymer Composites

Natural fibers are getting attention due to their ecofriendly nature and their sustainability. A comprehensive review has been presented of the widely used natural fiber reinforced polymer composites and their applications (87).

In addition, of various surface treatments applied to natural fibers were presented and their effect on natural fiber reinforced polymer composites properties. The properties of natural fiber reinforced polymer composites vary with fiber type and fiber source as well as fiber structure.

The chemical composition of some natural fibers is shown in Table 1.1.

Table 1.1 Chemical composition of natural fibers (87).

Fiber	Material/[%]			
	Cellulose	Hemicellulose	Lignin	Waxes
Bagasse	55.2	16.8	25.3	
Bamboo	26-43	30	21-31	
Flax	71	18.6-20.6	2.2	1.5
Kenaf	72	20.3	9	
Jute	61-71	14-20	12-13	0.5
Hemp	68	15	10	0.8
Ramie	68.6-76.2	13-16	0.6-0.7	0.3
Abaca	56-63	20-25	7-9	3
Sisal	65	12	9.9	2
Coir	32-43	0.15-0.25	40-45	
Oil palm	65	-	29	
Pineapple	81	-	12.7	
Curaua	73.6	9.9	7.5	
Wheat straw	38-45	15-31	12-20	
Rice husk	35-45	19-25	20	
Rice straw	41-57	33	8-19	8-38

The effects of various chemical treatments on the mechanical and thermal properties of natural fibers reinforcements thermosetting and thermoplastics composites were studied (87). A number of drawbacks of natural fiber reinforced polymer composites, like higher water absorption, inferior fire resistance, and lower mechanical properties limited its applications.

The impacts of chemical treatment on the water absorption, tribology, viscoelastic behavior, relaxation behavior, energy absorption flames retardancy, and biodegradability properties of natural fiber reinforced polymer composites were also presented.

Also, the applications of natural fiber reinforced polymer composites in automobile and construction industry and other applications were demonstrated (87).

The usage of natural fibers in industry is shown in Table 1.2.

It was concluded that a chemical treatment of the natural fiber improved the adhesion between the fiber surface and the polymer matrix, which ultimately enhanced the physicomechanical properties and the thermochemical properties of the natural fiber reinforced polymer composites.

Table 1.2 Natural fiber composite applications in industry (87, 89, 90).

Fiber	Usage
Hemp fiber	Construction products, textiles, cordage, geotextiles, paper & packaging, furniture, electrical, manufacture banknotes, and manufacture of pipes
Oil palm fiber	Building materials such as windows, door frames, structural insulated panel building systems, siding, fencing,roofing, decking, and other building materials
Wood fiber	Window frame, panels, door shutters, decking, railing systems, and fencing
Flax fiber	Window frame, panels, decking, railing systems, fencing, tennis racket, bicycle frame, fork, seat post, snow boarding, and lap top cases
Rice husk fiber	Building materials such as building panels, bricks, window frame, panels, decking, railing systems, and fencing
Bagasse fiber	Window frame, panels, decking, railing systems, and fencing
Sisal fiber	In construction industry such as panels, doors, shutting plate, and roofing sheets; also, manufacturing of paper and pulp
Stalk fiber	Building panel, furniture panels, bricks, and constructing drains and pipelines
Kenaf fiber	Packing material, mobile cases, bags, insulations, clothing-grade cloth, soilless potting mixes, animal bedding, and material that absorbs oil and liquids
Cotton fiber	Furniture industry, textile and yarn, goods, and cordage
Coir fibers	Building panels, flush door shutters, roofing sheets, storage tank, packing material, helmets and postboxes, mirrorcasing, paper weights, projector cover, voltage stabilizer cover, a filling material for the seat upholstery, brushes and brooms, ropes and yarns for nets, bags, and mats, as well as padding for mattresses, seat cushions
Ramie fiber	Use in products as industrial sewing thread, packing materials, fishing nets, and filter cloths. It is also made into fabrics for household furnishings (upholstery, canvas) and clothing, paper manufacture
Jute fiber	Building panels, roofing sheets, door frames, door shutters, transport, or packaging

1.6.2 Shape Memory Systems

PU shape memory polymers (SMPs) with tunable thermomechanical properties and advanced processing capabilities were synthesized and implemented in the design of a microactuator medical device prototype (88). The ability to manipulate glass transition temperature (T_g) and crosslinking density in low-molecular weight aliphatic thermoplastic PU SMPs was demonstrated using a synthetic approach that employs UV catalyzed thiol-ene click reactions to achieve a postpolymerization crosslinking (88).

To tailor the crosslinking density in the thiol-ene crosslinked PU SMP system, as alkene diol, trimethylolpropane allyl ether and as end-capping agent allyl alcohol was used.

To tailor the glass transition by varying the aliphatic diol co-monomer, diethylene glycol, 3-methyl-pentanediol, 1,4-butanediol, 2-methylpropanediol, 2,2´-dimethylpropanediol, and 1,4-cyclohexanedimethanol were used. These compounds are shown in Figure 1.18.

To tailor the glass transition by varying the diisocyanate monomer composition, hexamethylene diisocyanate, trimethylhexamethylene diisocyanate, and dicyclohexylmethane 4,4'-diisocyanate were used. These compounds are shown in Figure 1.19.

As polythiol crosslinking agents, ethylene glycol bis(3-mercaptopropionate) and dipentaerythritol hexakis(3-mercaptopropionate), trimethylolpropane tris(3-mercaptopropionate), tris[2-(3-mercaptopropionyloxy)ethyl] isocyanurate, and pentaerithritol tetrakis(3-mercaptopropionate) were used. These compounds are shown in Figure 1.20.

As photoinitiator, 2,2´-dimethoxy-2-phenylacetophenone, c.f. Figure 1.21, was used.

PUs containing varying C=C functionalization were synthesized, solution blended using polythiol crosslinking agents and photoinitiator and subjected to UV irradiation. The effects of number of synthetic parameters on crosslink density were reported. The thermomechanical properties are highly tunable, including glass transitions tailorable between 30 and 105 °C and the rubbery moduli are tailorable between 0.4 and 20 *MPa*.

This SMP system exhibits a high toughness for many formulations, especially in the case of low crosslink density materials, for

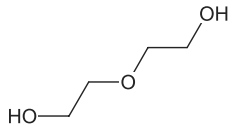

Diethylene glycol

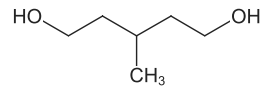

3-Methyl-pentanediol

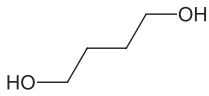

1,4-Butanediol

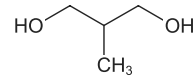

2-Methylpropanediol

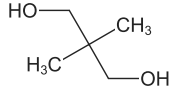

2,2´-Dimethylpropanediol

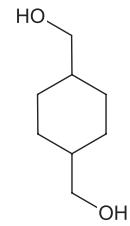

1,4-Cyclohexanedimethanol

Figure 1.18 Diols.

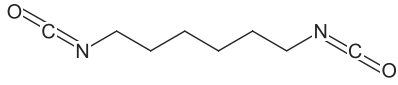

Dicyclohexylmethane 4,4´-diisocyanate

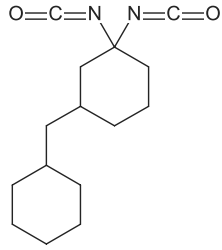

Hexamethylene diisocyanate

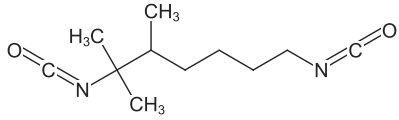

Trimethylhexamethylene diisocyanate

Figure 1.19 Diisocyanate monomers.

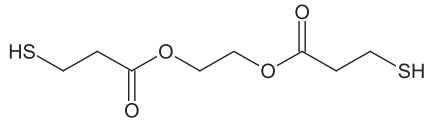

Ethylene glycol bis(3-mercaptopropionate)

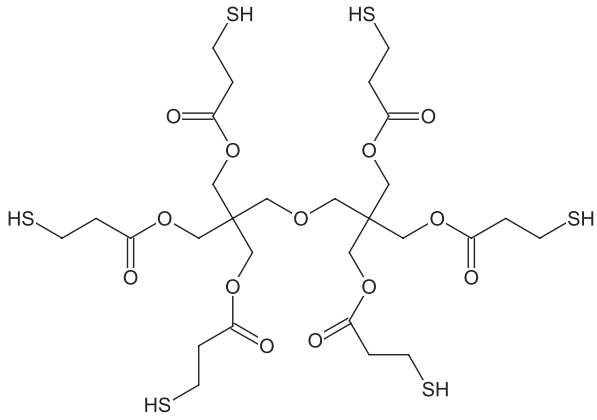

Dipentaerythritol hexakis(3-mercaptopropionate)

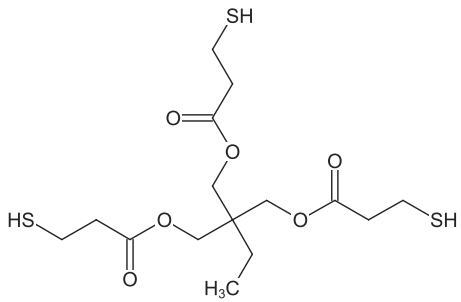

Trimethylolpropane tris(3-mercaptopropionate)

Figure 1.20 Polythiol crosslinking agents.

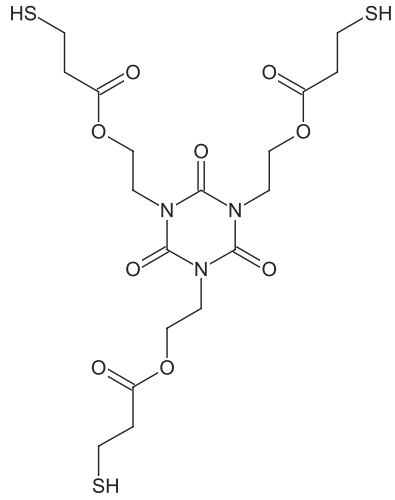

Tris[2-(3-mercaptopropionyloxy)ethyl] isocyanurate

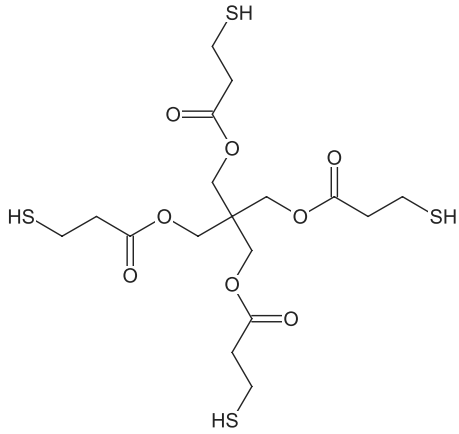

Pentaerithritol tetrakis(3-mercaptopropionate)

Figure 1.20 (cont) Polythiol crosslinking agents.

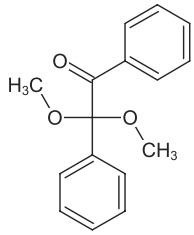

Figure 1.21 2,2´-Dimethoxy-2-phenylacetophenone.

which toughness exceeds 90 $MJ\,m^{-3}$ at the selected straining temperatures. To demonstrate the advanced processing capability and synthetic versatility of this SMP system, a laser-actuated SMP microgripper device for minimally invasive delivery of endovascular devices was fabricated. This system exhibited an average gripping force of $1.43 \pm 0.37\,N$. It could be successfully deployed in an *in vitro* experimental setup under simulated physiological conditions (88).

A simple method was tried to prepare thermoplastic poly(urethane) (TPU) PCL blends that possess shape memory attributes (91). These materials were melt compounded via a twin-screw extruder and injection molded at various ratios. Multiple test methods were used to characterize their shape memory properties and reveal the underling mechanism. The blends containing 25% TPU and 75% PCL exhibited the best shape memory properties as indicated by a 98% shape fixing ratio and 90% shape recovery ratio. This was attributed to the hybrid crystalline and amorphous regions of PCL and TPU.

It was also found that PCL and TPU has a good miscibility and that the PCL domain in TPU 25% had higher crystallinity than neat PCL. The crystalline region in TPU 25% could deform and maintain its temporary shape when stretched, which contributed to its high shape fixing attribute. On the other hand, the rubbery TPU region assisted in the recovery of the sample upon heating by releasing the deformation energy stored. Moreover, the TPU 25% string prepared could knot itself in a hot water bath, indicating a potential for suture applications. Lastly, the 3T3 fibroblast cells cultured on

the TPU/PCL blends showed high viability and active substrate-cell interactions (91). The term 3T3 refers to the abbreviation of 3-day transfer (92).

Biocompatible and biodegradable PU and PCL were blended to obtain shape-memory properties (93). Highly crystalline PCL was used as a hard segment, and PU synthesized from isosorbide, c.f. Figure 1.22, was used as a soft segment. The so obtained PU/PCL blends with the 30%, 50%, and 70% PU were investigated for their thermal properties, mechanical properties, and shape-memory behavior.

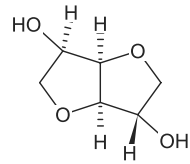

Figure 1.22 Isosorbide.

The 30%PU/PCL polymer showed the best shape-memory characteristics and could be knotted by itself in the hot water bath, indicating that it can be applied in smart suture applications. The degradation test performed at 37°C in phosphate buffered solution showed a mass loss of 2–4% for the obtained PU/PCL blends after 6 weeks (93).

1.6.3 Smart Polymers

The issues of smart polymers have been described in a monograph (94).

Smart polymers or stimuli-responsive polymers are high-performance polymers that change according to the environment they are in (95). Such materials can be sensitive to a number of factors, such as temperature, humidity, pH, chemical compounds , the wavelength or intensity of light or an electrical or magnetic field and can respond in various ways, like altering color or transparency, becoming conductive or permeable to water or changing the shape (shape memory polymers).

1.7 Porous Materials

1.7.1 Preparation Methods

1.7.1.1 Emulsion Templating

Emulsion templating can extend the fabrication of the original hydrophobic porous polymers that were synthesized within surfactant-stabilized water-in-oil high internal phase emulsions by using free radical polymerization (96). This perspective shows the extraordinary versatility of emulsion templating that has emerged with the growing numbers of high internal phase emulsion systems, high internal phase emulsion stabilization strategies, monomers, polymerization chemistries, multicomponent materials, and surface functionalities.

Emulsion templating now goes far beyond porous polymers by encompassing the encapsulation of aqueous solutions, ionic melts, and organic liquids as well as by encompassing porous carbons and porous inorganics (96).

The methods and monomers for synthesis are collected in Table 1.3.

Table 1.3 Methods and monomers for synthesis (96).

Polymerization methods	Monomers
Free radical polymerization	Acrylates, Styrenics
Step-growth polymerization (SGP)	Ureas, Urethanes
Click reaction	Azides, Thiol-enes
Reversible addition-fragmentation chain-transfer polymerization (RAFT)	Acrylamides
Ring-opening metathesis polymerization (ROMP)	Norbornadiene
Ring-opening polymerization (ROP)	Lactones
Atom transfer radical polymerization (ATRP)	Acrylates, Methacrylates

Much of the original work on high internal phase emulsion formation focused on water-in-oil high internal phase emulsions for hydrophobic polymer synthesis. In recent years, many novel high internal phase emulsion systems have been developed including

oil-in-water, supercritical carbon dioxide-in-water (97), and non-aqueous emulsions such as oil-in-oil (98), ionic liquid-in-oil (99), and oil-in-deep-eutectic solvent (100, 101).

A low-density, macroporous polymer is usually produced by formulating a stable high internal phase emulsion with a polymerizable continuous phase, polymerizing the continuous phase to *lock-in* the emulsion microstructure, and removing both the dispersed phase and the unreacted components of the continuous phase (102, 103).

A high internal phase emulsion stability, essential for polymer synthesis, can be enabled by a high internal phase emulsion stabilizer, which is usually a surfactant, but the stabilizer can also be amphiphilic particles and gels. The development of high internal phase emulsion stabilization strategies has recently attracted considerable attention as a means of manipulating the properties by manipulating the porous structure of the polymers (96).

1.7.1.2 Continuous Extrusion Foaming

Continuous extrusion processes are desirable because they can produce greater quantities of product in less time than, for example, batch processes (104, 105). The technology required for preparing nanofoam has proven to be challenging to be incorporated in a continuous extrusion process at least partially due to the amount and type of blowing agent required to prepare nanofoam.

Nanofoam has typically been prepared in batch processes using supercritical carbon dioxide, or a similar blowing agent, under extremely high pressures. A continuous extrusion foaming process has been presented that is using the following steps (105):

1. Providing a polymer melt in an extruder of an extrusion foaming line, the polymer melt comprising a polymer composition that has a softening temperature and that consists of all of the polymers in the polymer melt,
2. Introducing carbon dioxide into the polymer melt within the extrusion foaming line at an initial addition pressure while mixing the polymer melt and carbon dioxide together and while the polymer melt is at an initial addition temperature that is above the softening temperature of the polymer composition to form a polymer/carbon dioxide mixture wherein

the total amount of carbon dioxide added to the polymer melt exceeds the amount of carbon dioxide that is soluble in the polymer composition at the initial addition temperature and initial addition pressure and the carbon dioxide is dispersed throughout the polymer composition,

3. Cooling the polymer/carbon dioxide mixture to a dissolving temperature that is below the initial addition temperature while keeping the pressure around the polymer/carbon dioxide mixture between the initial addition pressure and a dissolving temperature that is equal to or below the initial addition pressure, wherein all of the carbon dioxide in the polymer/carbon dioxide mixture is soluble in the polymer composition at the dissolving temperature and dissolving pressure, and
4. Extruding the polymer/carbon dioxide mixture through an extrusion die into an expansion region having an expansion pressure that is lower than the dissolution pressure such that the polymer/carbon dioxide mixture experiences a pressure drop of at least 5 MPa MegaPascals at a rate of at least 10 $MPa\,s^{-1}$ as it exits the extrusion die and expands into a polymeric foam having an average transverse cell size that is less than one micrometer; wherein the process is free from adding solid carbon dioxide to the polymer and wherein the polymer/carbon dioxide mixture does not experience a pressure greater than the initial addition pressure during the extrusion foaming process.

Unlike a batch foam process, an extrusion process is particularly well suited for preparing a polymeric foam having cells that are elongated in the extrusion direction because the extrusion rate can be controlled, e.g., with pullers to enhance the foam translation in the extrusion direction), to enhance or diminish the aspect ratio of the cell sizes.

The polymeric foam desirably has a density of 0.5 $g\,cm^{-3}$ or less, most preferably 0.06 $g\,cm^{-3}$. The density is measured according to ASTM method D-1622-03 (106). The continuous polymeric foam also has a porosity of most preferably 85% or more.

The properties of a so prepared poly(methyl methacrylate) (PMMA) foam are shown in Table 1.4.

Table 1.4 Properties of a PMMA foam (105).

Property	Value	
Silicon dioxide nucleator	0	[%]
Initial Addition Temperature	172	[°C]
Initial Addition Pressure	46	[*MPa*]
Total Carbon Dioxide added	30	[%]
Approximate Carbon Dioxide Solubility limit in PMMA at initial addition temperature and pressure	13	[%]
Dissolving Temperature	41	[°C]
Dissolving Pressure	35	[*MPa*]
Approximate Carbon Dioxide Solubility limit in PMMA at dissolving temperature and pressure	33	[%]
Average transverse cell size	360	[*nm*]
Foam density	0.32	[$g\,cm^{-3}$]
Foam porosity	73.1	[%]
Area % cells > 1 μm	3	[%]

A feed with the PMMA a 2.5% loading relative to the PMMA weight of nucleator concentrate was fabricated. The nucleator concentrate is obtained by compounding silica nanoparticles, i.e., Aerosil 300 with ground PMMA powder in a 1:9 mass ratio. The resulting nucleator concentration in was 0.25% relative to PMMA (105).

Linear poly(propylene) (PP) foams, blown in a continuous extrusion process using supercritical CO_2 as the blowing agent, exhibited a poor cell morphology and a narrow foaming window, because of their low melt strength (107).

In a study, poly(tetrafluoroethylene) (PTFE) was blended with a PP resin with the aim of improving the foaming behavior of PP (107). It was found that the PTFE particles were deformed into fine fibers under shear or extensional flows during the extrusion process, which significantly increased the melt strength of PP from 0.005 N to 0.03 N (PP/PTFE with PTFE content of 4.0 wt %) at 230°C. These results indicated that the presence of PTFE improved the cell morphology of PP foams and broadened the foaming window of PP (107).

Open-cell PP/poly(oxyethylene) (POE) foams with different cell

structures were prepared by controlling the foaming temperature via a continuous extrusion foaming process. The effect of the cell structures on the sorption process, rate, and capacity was then studied (108). Pseudo-first order and pseudo-second order models were used to study the sorption kinetics of the PP/POE foams for cyclohexane.

The sorption rate and sorption capacity by both volume and weight of the PP/POE foam for different oils and solvents were studied to show how the intrinsic properties of the testing oils and solvents affected the sorption performance.

The results of the study showed that the sorption with the PP/POE foams followed the pseudo-second order kinetics model. Both the cell structures of the foams and the intrinsic properties of the testing oils and solvents affected the sorption performance.

For the same testing oil, a higher open-cell content in the foam was favorable for a higher sorption rate, and a higher void fraction was favorable for a higher sorption capacity. For the same foam, a lower viscosity of the testing oil was favorable for a higher sorption rate. The sorption capacity by volume was closely related to the viscosity of the testing oil, while both the viscosity and the density of the testing oil determined the sorption capacity by weight (108).

1.7.1.3 Steam-Chest Molding

Steam-chest molding can be used to prepare molded bead foams, including expandable PS, expanded PE, expanded PP, and expanded poly(lactic acid) with complex three-dimensional shapes. A new thermoplastic elastomer bead foam, expanded thermoplastic PU has been fabricated (109). This material has an excellent soft touch quality and is ductile. It has also generated widespread interest in both the academic and industrial communities.

Three types of foams with various sample sizes were steam-chest molded. Morphological observations showed that the interfaces of the expanded thermoplastic PU bead foams were effectively bonded. A high tensile strength of 1.80 *MPa* and an elongation at break of 360.1% were reached with a density of 0.35 $g\,cm^{-3}$.

A 200-fold cyclic compression measurement verified that the compressed METPU sample could recover more than 95% both in stress

and modulus, after 6 *d* of relaxation. This finding suggested the presence of an excellent interbead bonding in the PU bead foams (109).

1.7.1.4 High-Pressure Foam Injection Molding

A high-pressure foam injection molding process was used to fabricate microcellular high impact poly(styrene) (HIPS) foams with a tailored cellular structure (110). The process is cost-effective, highly efficient and flexible, and can be easily scaled up to complex components. The cellular structure of HIPS foam can be tuned over a wide range by manipulating packing time, cooling time, mold temperature, and mold-opening distance.

A microcellular HIPS foam with a weight reduction of up to 60% was prepared (110), which possesses a low thermal conductivity of 60 $mW\,m^{-1}K^{-1}$ and an ultra-low dielectric constant of 1.25. Both the thermal conductivity and the dielectric constant can be tailored by regulating the expansion ratio of HIPS foam. Mathematical models based on the mixing rule were developed to clarify the dependence of thermal conductivity and dielectric constant on the cellular structure of the foam.

The outstanding thermally and electrically insulating properties of HIPS foams come from a large amount of air in the microcellular structure. These lightweight, thermally insulating, and ultralow dielectric microcellular HIPS foams hold a great promise as an ultra-efficient insulating material for its use in many applications such as microelectronics and microelectromechanical systems (110).

1.7.1.5 Cationic Step-Growth Polymerization

The acid induced step-growth polymerization methods of bis(*p*-methoxybenzyl) carbonate (pMBC), bis(*m*-methoxybenzyl) carbonate (mMBC) and difurfuryl carbonate (DFC) have been used to produce resin-foams, because a controlled release of carbon dioxide takes place during the polymerization of those organic carbonates.

The monomers are polymerized in bulk using *p*-toluene sulfonic acid (pTS) as a catalyst. Furthermore, the volume development of the foams is assisted by use of an appropriate surfactant, Dabco® DC 193 and the crosslinking agent 1,3,5-trioxane as co-components.

(111)

1.7.2 Polymer Foams

The applications of polymer foams, and the properties that make them suitable for many applications have been described in a monograph (112).

1.7.2.1 Macroporous Polymers

Emulsions, foams, and foamed emulsions have been used successfully as templates for the synthesis of macroporous polymers. Based on this knowledge strategies to use these templating methods to synthesize tailor-made porous polymers have been reviewed (113).

The uniqueness of such polymers lies in the ability to tailor their structures and, therefore, their properties. However, systematic studies on structure-property relations are lacking mainly because the templating scientific community is split into two: The polydisperse and monodisperse camps.

In order to build a bridge between these camps, porous polymers may be synthesized with very different structures from the same precursors, to determine the relationship between the structure and the properties (113).

A variety of methods can be used to generate porous polymers: macromolecular design, i.e., porous frameworks, rigid structures with inherent microporosity, further porogen incorporation, phase inversion, and templating (102, 114–116).

1.7.2.2 Nanocellular Polymer Foam

Superinsulating materials are playing an important role in achieving the sustainable development of our modern world by improving energy efficiency, and reducing energy consumption and CO_2 emission (117). Nanocellular polymer foams have been considered as a promising superinsulating material, but their development is yet to be achieved. The understanding of thermal transport through the nanocellular foam is crucial for developing this superinsulating material.

An accurate mathematical model was reported to quantitatively estimate thermal transport through the nanocellular polymer foam (117). This is realized by taking into account the phonon scattering effect, the Knudsen effect and the thin-film interference effect in modelling the thermal transport through solid conduction, gas conduction and thermal radiation, respectively. A quantitative relationship could be shown between the cellular structure and the equivalent thermal conductivity.

The developed mathematical model offers a very useful tool for deeply understanding thermal transport through the nanocellular polymer foams, and guiding the development of the new generation of superinsulating materials (117).

1.7.2.3 Sound Absorption

A multi-walled carbon nanotube (MWCNT) composite foam from PU and poly(vinylidene fluoride) (PVDF) was designed and fabricated (118). The foam exhibited a high airborne sound absorption performance in a wide-frequency range.

The sound absorption coefficient reached the value of 0.85 at 1 *kHz*, which is a significant improvement over a conventional PU foam. It was found that PVDF formed a separate immiscible phase and part of it was crystallized in a polar phase in the PU scaffold in the PU/PVDF/MWCNT composite. This could benefit the sound absorption performance by introducing interfacial damping and local piezoelectric damping effects.

The introduction of the conductive MWCNT filament in the composite foam further improved the sound absorption, possibly by facilitating the dissipation of the electrical charges generated from local piezoelectric effect and enhancing both the interfacial damping effect and local piezoelectric damping effect. With PU as the main ingredient, the fabrication scalability of the foam can be improved with significantly reduced material and production cost in comparison to a PVDF foam (118).

1.7.2.4 Poly(urethane) Foam from Recycling

The recycling of flexible PU foam (PUF) was assessed using an ultrasonic reactor (119). Waste PU foam of automotive seat cushions

were subjected to ultrasonic horn oscillation of various amplitudes at different flow rate.

Successful decrosslinking of ultrasonically treated waste PU foam was confirmed by thorough characterizations such as gel fraction, crosslink density, and thermal property. Decrosslinked PU foams were blended with the virgin PU foam in various proportions to prepare the recrosslinked PU foams. Automotive seat cushions made of the blended PU foams exhibit enhanced comfort than that of the virgin PU foams by lowering the hardness and hysteresis loss and increasing the sag factor (119).

1.7.3 Porous Polymer Monoliths

Advanced porous materials with well-understood and enhanced properties have been elucidated in a a review for their implementations in the fields of life science and engineering (120, 121).

The current generation of porous organic monolithic materials as hierarchically structured materials has been described. The structure is derived from fundamental events occurring during preparation. Understanding the evolution of their porous structure from a free-radical crosslinking polymerization or copolymerization process gives an insight for an advanced understanding of structure-to-function relationships.

A number of existing and emerging characterization techniques and cross-correlation to synthetic design of experiments are also of importance. Some exciting new approaches for creation of porous polymer monoliths were discussed in the review, for example, living polymerization and routes based on click chemistry. Furthermore, it has been suggested that the new synthetic concepts must be accompanied with an advanced structural understanding of the materials to identify a desired step-change for their performance to be used in separations, catalysis, and extraction (120).

The incorporation of ionic liquids to increase the number of types of interaction mechanisms available for retention was also discussed (121). Monoliths affording molecular recognition properties achieved by including boronate moieties for cis-diol recognition, as well as antibodies and aptamers for specific molecular recognition are also reviewed. The largest number of applications

of molecular recognition mechanisms was observed for molecularly imprinted polymer monoliths as a consequence of the simplicity of this approach when compared to the use of immunosorbents or aptamers (121).

A novel route to prepare cellulose monoliths with hierarchically porous structure by selecting cellulose acetate as the starting material has been proposed (122).

A thermally induced phase separation of cellulose a acetate solution was done, using a mixed solvent. This affords a cellulose acetate monolith, which is converted into the cellulose monolith by alkaline hydrolysis.

SEM images of the cellulose acetate and cellulose monoliths showed a continuous macropore with a rough surface. Furthermore, nitrogen adsorption/desorption analysis indicated the formation of a mesoporous structure.

The macroporous structure could be controlled by changing the fabrication parameters. A series of reactive groups were introduced by chemical modifications on the surface of the cellulose monolith. The facile and diverse modifiability combined with its hydrophilic property make the hierarchically porous cellulose monolith a potential platform for its use in separation, purification and bio-related applications (122).

1.7.4 Concrete

1.7.4.1 Fibrous Light Weight Concrete

Fiber reinforced concrete are composite materials made with Portland cement, aggregate, and incorporation of discrete discontinuous fibers (123). Such fibers have been added to concrete because plain, unreinforced concrete is a brittle material, with a low tensile strength and a low strain capacity. The role of randomly distributed discontinuous fibers is to bridge across the cracks that provides some post-cracking (ductility). If the fibers are sufficiently ductile, the fibers could be capable of carrying significant stresses over a relatively large strain capacity in the post-cracking stage which characteristic is the case of corrugated steel fiber. The real contribution of the fibers is to increase the toughness of the concrete. Also, fibers tend to increase the strain at peak load and provide a great deal of

energy absorption in post-peak portion of the load vs. deflection curve and enhances ductility of virgin concrete.

When the fiber reinforcement is in the form of short discrete fibers, they act effectively as rigid inclusions in the concrete matrix. Physically, they have thus the same order of magnitude as aggregate inclusions; steel fiber reinforcement cannot therefore be regarded as a direct replacement of longitudinal reinforcement in reinforced and pre-stressed structural members. However, because of the inherent material properties of fiber concrete, the presence of fibers in the body of the concrete or the provision of a tensile skin of fiber concrete can be expected to improve the resistance of conventionally reinforced structural members to cracking, deflection and other serviceability conditions.

Light weight concrete is very helpful in reducing the weight of concrete and this perfect benefit leads to reduce the percentage of steel reinforcement in structural elements specially in the slabs. One of disadvantages of light weight concrete is its low compressive strength and the weakness behavior (123).

Glass fiber-reinforced polymer composites were fabricated and tested. The usage external glass fiber-reinforced polymer sheets enhanced compressive strength by 185% and 200% for fibrous traditional concrete and fibrous light weight concrete, respectively. It was recommended to use epoxy resin instead of polyester resin (123).

1.7.4.2 Porous Concrete

Porous concrete is a special type of an advanced concrete (124). It is a high porosity concrete used for outdoor flatwork. Porous concrete allows water to pass through it. It has a low water/cement ratio, low slump mix consisting of cement, narrowly graded coarse aggregate, little or no fine aggregate, water and admixtures.

The amount of water that is used in a mix is highly critical. Too much water will cause a segregation. On the other hand. little water will lead to a balling effect in the mixer and slow unloading times.

Some proportions of mixture that are suitable for porous concrete are collected in Table 1.5.

In the study, polymer impregnated concrete slab specimens were prepared (124). Cement mortar was used to cover the specimen from four sides and bottom of slab to act as a closed box. This

Table 1.5 Mixture proportions porous Concrete (124).

Material	Range (125)	Typical (125)	Range (126)
Cementitious Material /[$kg\,m^{-3}$]	270–415	325–400	224–388
Coarse Aggregate /[$kg\,m^{-3}$]	1190–1600	1400–1550	1431–1670
Water/cementitious Ratio	0.20–0.45	0.27–0.30	0.27–0.38
Admixtures /[$ml\,100kg^{-1}$]	200–400	300–	200–400
Permeability /[$l\ min^{-1}m^{-2}$]	100–900	500–	200–
Void Content /[%]	15–35	20–30	13–30

helped to fill slab specimens partially with resin (J-FIX Polyester Resin). The porosity of porous concrete was measured by filling the slab specimens with fully water and water volume was observed to obtain porosity and to ensure a closed box action before pouring resin. The detected value was approximately 30% of total volume of specimen.

The volume of resin was stacked in all slab specimens and covered by 75% of total volume of voids percentage. The pouring process was carried out regularly with different layers to ensure great integrity between concrete ingredients. Finally, specimens were tested under two static loads for flexure behavior.

So, a polymer impregnated porous concrete is a suitable solution for a low compressive strength problem. The experimental results showed that increasing the cement content cannot improve the behavior of polymer impregnated porous concretes lab, but it can affect the failure mode due to changing in displacement ductility factor because it gives a bond between ingredients and delay the cracking mode to appear in an early state (124).

1.7.4.3 Test Methods

ASTM standards for cement and concrete have been summarized (127).

The ASTM C1438-13 standard covers the performance criteria for latex and powder polymer modifiers for improving the adhesion and reducing permeability of hydraulic cement concrete and mortar (128). The polymer modifiers are classified either for general use or for use in areas not exposed to moisture and should be able to

produce test mortar or test concrete that conforms to the specified requirements.

The ASTM C1439-19 test methods are used to develop data for comparison with the requirements of Specification C1438 (129). Standardized procedures are used to compare the properties of specimens made from test mixtures of polymer-modified concrete or mortar with the properties of specimens made from reference mixtures. These test methods are not intended to simulate job conditions.

References

1. E.N. Peters, Thermoplastics, thermosets, and elastomers –descriptions and properties, 2015.
2. J.-C. Buffet, Z. Turner, and D. O'Hare, *Chem. Commun.*, Vol. 54, p. 10970, 2018.
3. A. Vantomme, P. Bernard, J. Michel, C. Willocq, and A. Sigwald, Metallocene-catalyzed polyethylene, US Patent 10 053 522, assigned to Total Research & Technology Feluy (Seneffe, BE), August 21, 2018.
4. A. Vantomme, E. Maizers, and C. Willocq, Metallocene-catalyzed polyethylene, US Patent 10 336 892, assigned to Total Research & Technology Feluy (Seneffe, BE), February 7, 2019.
5. Plastics – Methods for determining the density of non-cellular plastics – Part 1: Immersion method, liquid pycnometer method and titration method, ISO Standard 1183-1, International Organization for Standardization, Geneva, Switzerland, 2019.
6. T. Toda, I. Miura, M. Miya, and K. Takenaka, *Catalysts*, Vol. 9, p. 660, 2019.
7. K. Zhang, P. Liu, W.-J. Wang, B.-G. Li, W. Liu, and S. Zhu, *Macromolecules*, Vol. 51, p. 8790, 2018.
8. S.-M. Lai, P.-H. Huang, H.-C. Kao, and L.-C. Liu, *Journal of Macromolecular Science, Part B*, Vol. 56, p. 97, 2017.
9. I. Charitos, G. Georgousis, and E. Kontou, *Polymer Composites*, Vol. 40, p. E1263, 2019.
10. L. Li, Y. Wang, and Y. Zhu, *Journal of Coatings Technology and Research*, Vol. 15, p. 593, 2018.
11. A. Frank, M. Bredács, M. Brasch, G. Pinter, and D. Nitsche, Lifetime of polyethylene geomembranes for water proofing of tunnels from the perspective of polymer engineering, p. 6, Salzburg, Austria,

2015. ISRM Regional Symposium - EUROCK 2015, 7-10 October, International Society for Rock Mechanics and Rock Engineering.
12. M. Bredács, A. Frank, M. Brasch, G. Pinter, and D. Nitsche, Lifetime of polyethylene geomembranes for water proofing of tunnels from the perspective of polymer engineering, in *Eurorock 15*. 54th Geomechanics Colloquium, 2015.
13. R. Brentin, D. Bank, and M. Hus, Sps crystalline polymer: A new metallocene-catalyzed styrene engineering thermoplastic in G.M. Benedikt and B.L. Goodall, eds., *Metallocene Catalzed Polymers. Materials, Properties & Markets*, chapter 11, pp. 89–96. Plastics Design Library, Norwich, N.Y., 1990.
14. D. Bank, R. Brentin, and M. Hus, Sps crystalline polymer: A new material for automotive interconnect systems. SAE International Congress and Exposition, 1997. SAE Technical Paper 970305.
15. Z. Shi, F. Guo, Y. Li, and Z. Hou, *Journal of Polymer Science Part A: Polymer Chemistry*, Vol. 53, p. 5, 2015.
16. D.-Q. Peng, X.-W. Yan, S.-W. Zhang, and X.-F. Li, *Chinese Journal of Polymer Science*, Vol. 36, p. 222, 2018.
17. Z. Hou and Y. Wakatsuki, *Coordination Chemistry Reviews*, Vol. 231, p. 1, 2002.
18. Z. Hou, Y. Luo, and X. Li, *Journal of Organometallic Chemistry*, Vol. 691, p. 3114, 2006.
19. A.-S. Rodrigues and J.-F. Carpentier, *Coordination Chemistry Reviews*, Vol. 252, p. 2137, 2008.
20. X. Li, M. Nishiura, L. Hu, K. Mori, and Z. Hou, *Journal of the American Chemical Society*, Vol. 131, p. 13870, 2009.
21. E. Laur, A. Welle, A. Vantomme, J.-M. Brusson, J.-F. Carpentier, and E. Kirillov, *Catalysts*, Vol. 7, p. 361, November 2017.
22. G. Droval, J.-F. Feller, P. Salagnac, and P. Glouannec, *Polymers for Advanced Technologies*, Vol. 17, p. 732, 2006.
23. V.L. Shangankuli, J.P. Jog, and V.M. Nadkani, *J. Appl. Polym. Sci.*, Vol. 36, p. 335, 1988.
24. M. Dasog, J. Kehrle, B. Rieger, and J.G.C. Veinot, *Angewandte Chemie International Edition*, Vol. 55, p. 2322, 2016.
25. S. Kano, K. Kim, and M. Fujii, *ACS Sensors*, Vol. 2, p. 828, 2017.
26. R.M. Hill, ed., *Silicone Surfactants*, Marcel Dekker, New York, 2019.
27. J. Chen, J.D. Fine, and C.A. Mullin, *Science of The Total Environment*, Vol. 612, p. 415, 2018.
28. Y. Huang, L. Meng, M. Guo, P. Zhao, H. Zhang, S. Chen, J. Zhang, and S. Feng, *Langmuir*, Vol. 34, p. 4382, 2018.
29. M. Zieba, A. Malysa, and E. Klimaszewska, *Tribology Transactions*, Vol. 60, p. 106, 2017.
30. F.M. Menger and C.A. Littau, *Journal of the American Chemical Society*, Vol. 113, p. 1451, 1991.

31. R. Zana, *Advances in Colloid and Interface Science*, Vol. 97, p. 205, 2002.
32. M. ud din Parray, M.U.H. Mir, N. Dohare, N. Maurya, A.B. Khan, M.S. Borse, and R. Patel, *Journal of Molecular Liquids*, Vol. 260, p. 65, 2018.
33. T. Jain, A.R. Tehrani-Bagha, H. Shekhar, R. Crawford, E. Johnson, K. Nørgaard, K. Holmberg, P. Erhart, and K. Moth-Poulsen, *J. Mater. Chem. C*, Vol. 2, p. 994, 2014.
34. Y. Bao, Y. Zhang, J. Guo, J. Ma, and Y. Lu, *Journal of Cleaner Production*, Vol. 206, p. 430 , 2019.
35. D.D. Pukale, A.S. Bansode, D.V. Pinjari, R.R. Kulkarni, and U. Sayed, *Journal of Surfactants and Detergents*, Vol. 20, p. 287, 2017.
36. L. Fang, J. Tan, Y. Zheng, G. Yang, J. Yu, and S. Feng, *Journal of Molecular Liquids*, Vol. 231, p. 134, 2017.
37. R. Deng, W. Zuo, J. Ku, Z. Yang, and Y. Hu, *International Journal of Mineral Processing*, Vol. 167, p. 113 , 2017.
38. G. Bhattacharjee, V. Barmecha, O.S. Kushwaha, and R. Kumar, *The Journal of Chemical Thermodynamics*, Vol. 117, p. 248, 2018. Special issue on Gas Hydrates.
39. L. Heisler, G.A. Pickrell, and L.F. Lawler, Silicone surfactant for use in polyurethane foams prepared using vegetable oil based polyols, US Patent 9 587 068, assigned to Momentive Performance Materials Inc. (Waterford, NY), March 7, 2017.
40. L. Heisler, G.A. Pickrell, L.F. Lawler, and J.C. Graham, Supercapacitor-emulating fast-charging batteries and devices, US Patent Application 2 007 029 359, assigned to General Electric Co., December 20, 2007.
41. Y. Sheng, X. Wu, S. Lu, and C. Li, *Journal of Surfactants and Detergents*, Vol. 19, p. 823, 2016.
42. M.F. Khan, L. Zepeda-Velazquez, and M.A. Brook, *Colloids and Surfaces B: Biointerfaces*, Vol. 132, p. 216, 2015.
43. M.F. Khan, *The Antibacterial Activity of Silicone-Polyether Surfactants*. PhD thesis, McMaster University, Hamilton, Ontario, Canada, 2017, https://macsphere.mcmaster.ca/bitstream/11375/21971/2/Khan_Madiha_F_finalsubmission2017June_PhD.pdf.
44. F. Gonzaga, J.B. Grande, and M.A. Brook, *Chemistry – A European Journal*, Vol. 18, p. 1536, 2012.
45. M.F. Khan, N. Luong, J. Kurian, and M.A. Brook, *Chem. Commun.*, Vol. 53, p. 3050, 2017.
46. Y. Wei, C. Zheng, Z. Zhang, Z. Zeng, T. Mao, S. Long, and H. Ling, *Journal of Surfactants and Detergents*, Vol. 22, p. 285, 2019.
47. Wikipedia contributors, Self-healing material — Wikipedia, the free encyclopedia, https://en.wikipedia.org/w/index.php?title=Self-healing_material&oldid=921983255, 2019. [Online; accessed 10-November-2019].

48. M.Q. Zhang and M.Z. Rong, *Self-healing Polymers and Polymer Composites*, Wiley, Hoboken, N.J, 2011.
49. W. Binder, ed., *Self-healing polymers: From principles to applications*, Wiley-VCH, Weinheim, Germany, 2013.
50. G.L. und Harper Meng, ed., *Recent Advances in Smart Self-Healing Polymers and Composites*, Woodhead Publishing, an imprint of Elsevier Ltd, Cambridge UK, 2015.
51. M. Ramesh, L.R. Kumar, A. Khan, and A.M. Asiri, 22 self-healing polymer composites and its chemistry in A. Khan, M. Jawaid, S.N. Raveendran, and A.M. Asiri, eds., *Self-Healing Composite Materils. From Design to Application*, chapter 22, pp. 415–428. Woodhead Publishing, Cambridge. MA, 2019.
52. E.B. Murphy and F. Wudl, *Progress in Polymer Science*, Vol. 35, p. 223, 2010. Special Issue on Stimuli-Responsive Materials.
53. Y. Yang and M.W. Urban, *Chem. Soc. Rev.*, Vol. 42, p. 7446, 2013.
54. C. Dry, *Composite Structures*, Vol. 35, p. 263, 1996.
55. S.H. Cho, H.M. Andersson, S.R. White, N.R. Sottos, and P.V. Braun, *Advanced Materials*, Vol. 18, p. 997, 2006.
56. S.R. White, N.R. Sottos, P.H. Geubelle, J.S. Moore, M.R. Kessler, S.R. Sriram, E.N. Brown, and S. Viswanathan, *Nature*, Vol. 409, p. 794, 2001.
57. K.S. Toohey, N.R. Sottos, J.A. Lewis, J.S. Moore, and S.R. White, *Nature Materials*, Vol. 6, p. 581, 2007.
58. S.R. White, J.S. Moore, N.R. Sottos, B.P. Krull, W.A. Santa Cruz, and R.C.R. Gergely, *Science*, Vol. 344, p. 620, 2014.
59. E.L. Kirkby, J.D. Rule, V.J. Michaud, N.R. Sottos, S.R. White, and J.-A.E. Manson, *Advanced Functional Materials*, Vol. 18, p. 2253, 2008.
60. Y.-X. Lu and Z. Guan, *Journal of the American Chemical Society*, Vol. 134, p. 14226, 2012.
61. J. Canadell, H. Goossens, and B. Klumperman, *Macromolecules*, Vol. 44, p. 2536, 2011.
62. Y. Amamoto, H. Otsuka, A. Takahara, and K. Matyjaszewski, *Advanced Materials*, Vol. 24, p. 3975, 2012.
63. P. Zheng and T.J. McCarthy, *Journal of the American Chemical Society*, Vol. 134, p. 2024, 2012.
64. L. He, D.E. Fullenkamp, J.G. Rivera, and P.B. Messersmith, *Chem. Commun.*, Vol. 47, p. 7497, 2011.
65. X. Chen, M.A. Dam, K. Ono, A. Mal, H. Shen, S.R. Nutt, K. Sheran, and F. Wudl, *Science*, Vol. 295, p. 1698, 2002.
66. F. Herbst, D. Döhler, P. Michael, and W.H. Binder, *Macromolecular Rapid Communications*, Vol. 34, p. 203, 2013.
67. M. Burnworth, L. Tang, J.R. Kumpfer, A.J. Duncan, F.L. Beyer, G.L. Fiore, S.J. Rowan, and C. Weder, *Nature*, Vol. 472, p. 334, 2011.

68. S. Bode, L. Zedler, F.H. Schacher, B. Dietzek, M. Schmitt, J. Popp, M.D. Hager, and U.S. Schubert, *Advanced Materials*, Vol. 25, p. 1634, 2013.
69. M. Nakahata, Y. Takashima, H. Yamaguchi, and A. Harada, *Nature Communications*, Vol. 2, p. 511, 2011.
70. S. Burattini, B.W. Greenland, D.H. Merino, W. Weng, J. Seppala, H.M. Colquhoun, W. Hayes, M.E. Mackay, I.W. Hamley, and S.J. Rowan, *Journal of the American Chemical Society*, Vol. 132, p. 12051, 2010.
71. J. Kalista, Stephen J., T.C. Ward, and Z. Oyetunji, *Mechanics of Advanced Materials and Structures*, Vol. 14, p. 391, 2007.
72. P. Cordier, F. Tournilhac, C. Soulié-Ziakovic, and L. Leibler, *Nature*, Vol. 451, p. 977, 2008.
73. T. Aida, E.W. Meijer, and S.I. Stupp, *Science*, Vol. 335, p. 813, 2012.
74. J. Hentschel, A.M. Kushner, J. Ziller, and Z. Guan, *Angewandte Chemie International Edition*, Vol. 51, p. 10561, 2012.
75. Y. Chen, A.M. Kushner, G.A. Williams, and Z. Guan, *Nature Chemistry*, Vol. 4, p. 467, 2012.
76. D. Mozhdehi, S. Ayala, O.R. Cromwell, and Z. Guan, *Journal of the American Chemical Society*, Vol. 136, p. 16128, 2014.
77. A.M. Kushner and Z. Guan, Synthesis of multiphase self-healing polymers from commodity monomers, US Patent Application 20 180 171 055, assigned to The Regents of the University of California, Oakland (CA), June 21, 2018.
78. A.M. KUSHNER and Z. Guan, Synthesis of multiphase self-healing polymers from commodity monomers, WO Patent 2 017 034 660, assigned to The Regents Of The University Of California, March 02, 2017.
79. J.-K. Wang, Q. Zhou, J.-P. Wang, S. Yang, and G.L. Li, *Colloids and Surfaces A: Physicochemical and Engineering Aspects*, Vol. 569, p. 52, 2019.
80. F. Bai, X. Yang, R. Li, B. Huang, and W. Huang, *Polymer*, Vol. 47, p. 5775, 2006.
81. D.J. Boday and T.C. Mauldin, Catalyst-lean, microcapsule-based self-healing materials via ring-opening metathesis polymerization (romp), US Patent 9 663 610, assigned to International Business Machines Corporation (Armonk, NY), May 30, 2017.
82. S.T. Jolley, M.K. Williams, T.L. Gibson, T.M. Smith, A.J. Caraccio, and W. Li, Self-healing polymer materials for wire insulation, polyimides, flat surfaces, and inflatable structures, US Patent 10 174 198, assigned to The United States of America as Represented by the Administrator of NASA (Washington, DC, US), August 1, 2019.
83. X. Cui, Y. Song, J.-P. Wang, J.-K. Wang, Q. Zhou, T. Qi, and G.L. Li, *Polymer*, Vol. 174, p. 143 , 2019.

84. Y. Yang, D. Davydovich, C.C. Hornat, X. Liu, and M.W. Urban, *Chem*, Vol. 4, p. 1928, 2018.
85. S. Zechel, M. Hager, T. Priemel, and M. Harrington, *Biomimetics*, Vol. 4, p. 20, February 2019.
86. G.R. Whittell, M.D. Hager, U.S. Schubert, and I. Manners, *Nature Materials*, Vol. 10, p. 176, 2011.
87. L. Mohammed, M.N.M. Ansari, G. Pua, M. Jawaid, and M.S. Islam, *International Journal of Polymer Science*, Vol. 2015, p. 1, 2015.
88. K. Hearon, M.A. Wierzbicki, L.D. Nash, T.L. Landsman, C. Laramy, A.T. Lonnecker, M.C. Gibbons, S. Ur, K.O. Cardinal, T.S. Wilson, K.L. Wooley, and D.J. Maitland, *Advanced Healthcare Materials*, Vol. 4, p. 1386, 2015.
89. T. Sen and H.N.J. Reddy, *International Journal of Innovation, Management and Technology*, Vol. 2, p. 192, 2011.
90. U.S. Bongarde and V.D. Shinde, *International Journal of Engineering Science and Innovative Technology*, Vol. 3, p. 431, 2014.
91. X. Jing, H.-Y. Mi, H.-X. Huang, and L.-S. Turng, *Journal of the Mechanical Behavior of Biomedical Materials*, Vol. 64, p. 94, 2016.
92. Wikipedia contributors, 3T3 cells — Wikipedia, the free encyclopedia, https://en.wikipedia.org/w/index.php?title=3T3_cells&oldid=843362440, 2018. [Online; accessed 27-September-2019].
93. Y.-S. Joo, J.-R. Cha, and M.-S. Gong, *Materials Science and Engineering: C*, Vol. 91, p. 426, 2018.
94. M.R. Aguilar and J. San Román, eds., *Smart Polymers and Their Applications*, Woodhead Publishing Series in Materials, Woodhead Publishing, Duxford, 2nd edition, 2019.
95. Wikipedia contributors, Smart polymer — Wikipedia, the free encyclopedia, https://en.wikipedia.org/w/index.php?title=Smart_polymer&oldid=890587556, 2019. [Online; accessed 27-September-2019].
96. T. Zhang, R. Sanguramath, S. Israel, and M.S. Silverstein, *Macromolecules*, Vol. 52, p. 5445, 2019.
97. W. Luo, S. Zhang, P. Li, R. Xu, Y. Zhang, L. Liang, C.D. Wood, Q. Lu, and B. Tan, *Polymer*, Vol. 61, p. 183, 2015.
98. E. Kot, N. Shirshova, A. Bismarck, and J.H.G. Steinke, *RSC Adv.*, Vol. 4, p. 11512, 2014.
99. N. Shirshova, P. Johansson, M.J. Marczewski, E. Kot, D. Ensling, A. Bismarck, and J.H.G. Steinke, *J. Mater. Chem. A*, Vol. 1, p. 9612, 2013.
100. M.G. Pérez-García, A. Carranza, J.E. Puig, J.A. Pojman, F. del Monte, G. Luna-Bárcenas, and J.D. Mota-Morales, *RSC Adv.*, Vol. 5, p. 23255, 2015.
101. A. Carranza, K. Song, J.F.A. Soltero-Martínez, Q. Wu, J.A. Pojman, and J.D. Mota-Morales, *RSC Adv.*, Vol. 6, p. 81694, 2016.

102. M.S. Silverstein, *Progress in Polymer Science*, Vol. 39, p. 199, 2014.
103. M.S. Silverstein, *Polymer*, Vol. 126, p. 261, 2017.
104. S. Costeux, D.R. Lantz, D.A. Beaudoin, and M.A. Barger, Continuous process for extruding nanoporous foam, US Patent 9 145 478, assigned to Dow Global Technologies LLC (Midland, MI), September 29, 2015.
105. S. Costeux, D.R. Lantz, D.A. Beaudoin, and M.A. Barger, Continuous process for extruding nanoporous foam, WO Patent 2 013 048 760, assigned to Dow Global Technologies LLC (Midland, MI), April 04, 2013.
106. Standard test method for apparent density of rigid cellular plastics, ASTM Standard D1922-09, ASTM International, West Conshohocken, PA, 2014. http://www.astm.org/cgi-bin/resolver.cgi?D1622D1622M-14.
107. K. Wang, F. Wu, W. Zhai, and W. Zheng, *Journal of Applied Polymer Science*, Vol. 129, p. 2253, 2013.
108. Y. Pang, S. Wang, M. Wu, W. Liu, F. Wu, P.C. Lee, and W. Zheng, *Polymers for Advanced Technologies*, Vol. 29, p. 1313, 2018.
109. C. Ge, Q. Ren, S. Wang, W. Zheng, W. Zhai, and C.B. Park, *Chemical Engineering Science*, Vol. 174, p. 337 , 2017.
110. G. Wang, G. Zhao, G. Dong, L. Song, and C.B. Park, *J. Mater. Chem. C*, Vol. 6, p. 12294, 2018.
111. L. Wöckel, A. Seifert, C. Mende, I. Roth-Panke, L. Kroll, and S. Spange, *Polymer Chemistry*, Vol. 8, p. 404, 2017.
112. N. Mills, *Polymer Foams Handbook: Engineering and Biomechanics Applications and Design Guide*, Elsevier, Amsterdam, 2007.
113. C. Stubenrauch, A. Menner, A. Bismarck, and W. Drenckhan, *Angewandte Chemie International Edition*, Vol. 57, p. 10024, 2018.
114. D. Wu, F. Xu, B. Sun, R. Fu, H. He, and K. Matyjaszewski, *Chemical Reviews*, Vol. 112, p. 3959, 2012.
115. M.T. Gokmen and F.E.D. Prez, *Progress in Polymer Science*, Vol. 37, p. 365, 2012. Topical Issue on Nanomaterials.
116. S. Qiu and T. Ben, *Porous Polymers: Design, Synthesis and Applications*, Royal Society of Chemistry, 2015.
117. G. Wang, C. Wang, J. Zhao, G. Wang, C.B. Park, and G. Zhao, *Nanoscale*, Vol. 9, p. 5996, 2017.
118. E.C. Statharas, K. Yao, M. Rahimabady, A.M. Mohamed, and F.E.H. Tay, *Journal of Applied Polymer Science*, Vol. 136, p. 47868, 2019.
119. J. Moon, S.B. Kwak, J.Y. Lee, D. Kim, J.U. Ha, and J.S. Oh, *Waste Management*, Vol. 85, p. 557, 2019.
120. I. Nischang and T.J. Causon, *TrAC Trends in Analytical Chemistry*, Vol. 75, p. 108, 2016.
121. J.C. Masini and F. Svec, *Analytica Chimica Acta*, Vol. 964, p. 24, 2017.

122. Y. Xin, Q. Xiong, Q. Bai, M. Miyamoto, C. Li, Y. Shen, and H. Uyama, *Carbohydrate Polymers*, Vol. 157, p. 429, 2017.
123. S. Yehia, *International Journal of Innovative Science, Engineering & Technology*, Vol. 119, p. 113, May 2015.
124. S. Yehia and M.M. Fawzy, *International Journal of Current Engineering and Technology*, Vol. 7, p. 431, April 2017.
125. Pervious concrete mix proportioning technical bulletin, Technical Report TB-0111, GCP-Applied Technologies, Inc., Cambridge, MA. Howpublished: https://gcpat.com/en/solutions/products/adva-high-range-water-reducers/tb-0111-pervious-concrete-mix-proportioning.
126. I.G. Axim, Practical application of previous concrete, in R. Blackburn, ed., *Pervious Concrete, Practical Application of Pervious Concrete: Mix Designs that are Workable*, pp. 1–20. NRMCA Conference, Axim Italcementi Group, 2006.
127. ASTM, Cement and concrete standards, Electronic: https://www.astm.org/Standards/cement-and-concrete-standards.html, 2019.
128. Standard specification for latex and powder polymer modifiers for use in hydraulic cement concrete and mortar, ASTM Standard C1438-13, ASTM International, West Conshohocken, PA, 2017. https://www.astm.org/Standards/C1438.htm.
129. Standard test methods for evaluating latex and powder polymer modifiers for use in hydraulic cement concrete and mortar, ASTM Standard C1439-19, ASTM International, West Conshohocken, PA, 2019. https://www.astm.org/Standards/C1439.htm.